INVESTIGATION OF THE ELASTIC PROPERTIES
OF LiKSO$_4$ SINGLE CRYSTALS AS A
FUNCTION OF TEMPERATURE AND PRESSURE

MAHMOUD ABU-KHARMA

INFORMATION TO USERS

This manuscript has been reproduced from the microfilm master. UMI films the text directly from the original or copy submitted. Thus, some thesis and dissertation copies are in typewriter face, while others may be from any type of computer printer.

The quality of this reproduction is dependent upon the quality of the copy submitted. Broken or indistinct print, colored or poor quality illustrations and photographs, print bleedthrough, substandard margins, and improper alignment can adversely affect reproduction.

In the unlikely event that the author did not send UMI a complete manuscript and there are missing pages, these will be noted. Also, if unauthorized copyright material had to be removed, a note will indicate the deletion.

Oversize materials (e.g., maps, drawings, charts) are reproduced by sectioning the original, beginning at the upper left-hand corner and continuing from left to right in equal sections with small overlaps.

Canada

Investigation of the Elastic Properties of LiKSO₄ Single Crystals as a Function of Temperature and Pressure

by

© Mahmoud Abu-Kharma

M.Sc. (1982) Jordan University, B.Sc. (1978) Jordan University

A thesis submitted to the
School of Graduate Studies
in partial fulfillment of the
requirements for the degree of
Master of Science.

Department of Physics and Physical Oceanography
Memorial University of Newfoundland

May 22, 2002

Contents

Abstract

The ultrasonic pulse-echo method is used to study the elastic properties of LiKSO$_4$ single crystals as a function of temperature between 4 K and 300 K and at pressures up to 7 kbar. The measured values of the elastic constants obtained at room temperature for the hexagonal phase structure are: C_{66}=1.41±0.03, C_{44}=2.11±0.04, C_{11}=5.7±0.1, C_{12}=2.92±0.06, and C_{33}=6.7±0.1 (×10^{10} N/m). At ambient pressure, phase transitions between 130 K and 300 K have been detected using the measurement of the relative change in sound velocity $\Delta v/v$ in both x- and z-directions for longitudinal modes. First order transitions are observed around 195 K and 185 K on cooling, and around 195 K and 260 K on heating. Relying on the measurements of $\Delta v/v$ in the x-direction for longitudinal modes in the same temperature range at different pressures, we derive the pressure-temperature phase diagram. The main features obtained for this diagram are: we observe a triple point at (1.8 kbar, 200 K) during the cooling process that shifts to (5 kbar, 286 K) for the heating, the intermediate phase PIV vanishes beyond the triple point, and the transition temperature is shifted to higher values with increasing pressures. In the temperature region below 130 K, we observed at low pressures phase transitions at 35 K and 65 K, with no sign of thermal hysteresis. However, for pressures greater than 3.2 kbar the transition observed at 35 K is suppressed. The existence of the phases PIII, PIV, PV, PIX and PX were confirmed. There were no transitions observed at 165 K, 135 K and 80 K, so we cannot confirm the PVI, PVII and PVIII phases.

v

Acknowledgements

List of Tables

List of Figures

Chapter 1

Introduction

1.1 Preface

In the last century, the interest in lithium potassium sulphate $LiKSO_4$ crystals has increased for several reasons. $LiKSO_4$ crystals exhibit a sequence of very interesting phase transitions between 20 K and 1000 K [1–4], and these phases display a variety of physical properties including, for example, ferroelectric behavior, ferroelastic behavior and the electro-optic effect. Large single crystals are relatively easy to grow, the material is stable, and the crystals survive first-order structural phase transitions without breaking [5].

Phase transitions have been studied by means of different techniques, such as thermal expansion measurements [6, 7], laser Raman spectroscopy [8–16], Brillouin scattering [2–4, 17–21], electrical studies [4, 7, 22–28], X-ray diffraction studies [29–40], ac calorimetry and differential scanning calorimetry (DSC) [22, 41, 42], neutron scattering [43–49], electron spin resonance (ESR) [50, 51], elastic properties [52–54], torsion vibration technique [54], crystal optical studies [55–59], nuclear magnetic resonance (NMR) [60], electron paramagnetic resonance (EPR) [61–67], resonant ul-

trasound spectroscopy (RUS) [5], acoustic studies [68-73], and infrared spectroscopy studies [74]. Nevertheless, the sequence of phase transitions, their temperatures, and the nature of the structural phase transitions are still not very well understood [1, 3, 4, 10, 17, 19, 20, 52, 56, 60, 67, 75]. This project will try to resolve some of these controversies regarding the sequence of phase transitions, especially below 160 K.

1.2 Overview of the Present Work

Up to now, some detailed studies of acoustic properties of LiKSO$_4$ have been performed for the high temperature range 300-900 K [69, 70, 73], and some for a low temperature range 165-300 K [5, 50, 68, 71, 72]. None of the previous investigations have successfully measured the elastic properties of LiKSO$_4$ below 160 K using acoustic methods. Consequently, the purpose of this project is to use the pulse echo method to measure the elastic properties of LiKSO$_4$ using acoustic waves propagating along different crystal directions in the temperature range between 4 K and 300 K. Moreover, most studies on LiKSO$_4$ crystals have been performed as a function of temperature only. Little has been reported on the pressure dependence of the properties of LiKSO$_4$ [24, 26, 76-79]. Accordingly, the behavior of lithium potassium sulphate under pressure is not well known. Therefore, we have also investigated the temperature dependence of the velocity of longitudinal sound waves propagating along the x-axis at different pressures. From these results, the pressure-temperature phase diagram is derived in the range between 130 K and 300 K, and compared to the phase diagram determined by strain $\frac{\Delta l}{l}$ measurements in the [001] direction [24, 26]. Finally, we will focus on the effect of both pressure and temperature on the sound velocity below 80 K.

1.3   Outline of the Thesis

The thesis consists of six chapters. An introduction, overview and outline of the thesis have been presented in Chapter One. Chapter Two presents the crystal structure of $LiSO_4$ and the results of previous acoustic studies. The background theory is presented in Chapter Three, where we discuss crystal elasticity and plane wave propagation in the crystals. The experimental setup and the principles used in these experiments are described in Chapter Four. Chapters Five and Six cover the results and conclusions, respectively. In the end a number of recommendations are listed.

Chapter 2

Crystal Structure

In this chapter, we will present the crystal structure of LiKSO$_4$, the crystal phases below room temperature, the physical properties, and finally review previous acoustic studies used to study the phase transitions in this material.

2.1   Lithium Potassium Sulphate Crystal LiKSO$_4$

LiKSO$_4$ crystals belong to the family of crystals with the general formula A'A''BX$_4$, where A' = Li, Na, A'' = Na, K, Rb, Cs, NH$_4$, N(CH$_3$)$_4$, N$_2$H$_5$ etc.. and BX$_4$ = SO$_4$, SeO$_4$, ZnCl$_4$, ZnBr$_4$, BeF$_4$, MnO$_4$, WO$_4$, etc., [6, 33, 57, 58, 67, 68, 80]. The A'A''BX$_4$ compounds share a high-temperature disordered phase belonging to the hexagonal space group P6$_3$ [34, 67]. The AX$_4$ and BX$_4$ tetrahedra form an ordered three dimensional framework structure characterized by six-membered rings of three AX$_4$ and three BX$_4$ tetrahedra. The apices of the three AX$_4$ tetrahedra point in the opposite direction from those of the three BX$_4$ tetrahedra. Different arrangements and deformations of the tetrahedra in these rings lead to different space groups for ideal crystal structure, so that LiKSO$_4$ undergoes several phase transitions [53, 80].

2.2 Crystal Structure

The crystal structure of LiKSO$_4$ was determined at room temperature by Bradley [29]. It crystallizes in the hexagonal system with space group P6$_3$, and is polar [7, 29, 32]. The unit cell is a prism containing two molecules [29, 33] and the lattice parameters are a = 5.147 Å and c = 8.633 Å [30, 53] which give an axial ratio c/a equal to 1.6773. The volume of the unit cell is 197.952 Å^3 with a density of 2384 kg/m^3 for LiKSO$_4$ [33]. The sulphate group SO$_4$ is considered to form a regular tetrahedron [7]. the SO$_4$ and LiO$_4$ tetrahedra form an ordered three dimensional framework structure characterized by six membered rings of three SO$_4$ and three LiO$_4$ tetrahedra. The apices of the three LiO$_4$ tetrahedra point in opposite direction from those of the three SO$_4$ tetrahedra. The lithium ion is surrounded by oxygen atoms located at a slightly distorted tetrahedra, and the potassium ions occupy positions on the hexagonal c axis and each is surrounded by nine nearest-neighbour oxygen atoms [29]. The hexagonal structure and the projections on the basal plane (0001) of LiKSO$_4$ are shown in Fig. 2.1.

2.2.1 Crystal Phases

We will study the phases of lithium potassium sulphate crystals in the temperature range between 4 K and 300 K. Therefore, we will briefly discuss the transitions below room temperature. First we will focus on the results obtained by different investigators in the temperature range between 170 K and 300 K. Then we will summarize the results obtained below 170 K.

In general, one can see from Fig. 2.2 several phases proposed according to results obtained by Leitao et al. [57], Zhang et al. [74], Liu et al. [80], Desert et al. [37], de Sousa et al. [28], Perpetuo et al. [67], etc. The first transition below
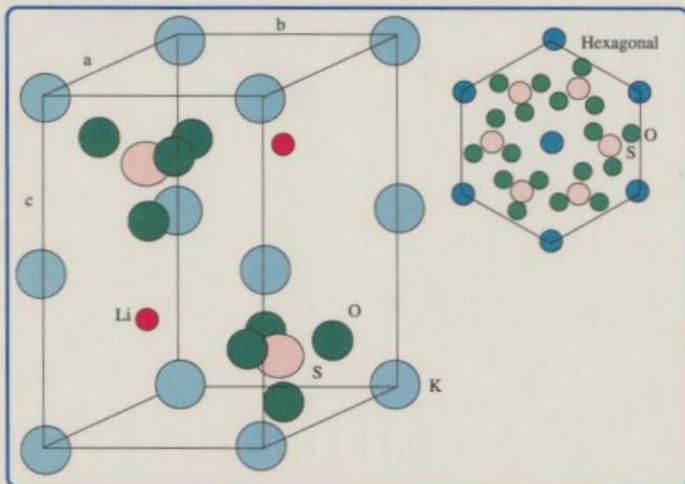
Figure 2.1: Schematic diagram of the arrangement of atoms in the room temperature hexagonal unit cell of LiKSO$_4$ and relative orientations of the SO$_4$ tetrahedra in the space group P6$_3$.

room temperature occurs around 205 K followed by another one at around 190 K. However, the interpretation of the experimental data has been conflicting such that the transition temperatures are not completely justified, and the crystal structure is not clearly defined except at room temperature. On the one hand, Raman scattering results indicate a phase change from hexagonal to trigonal at 201 K on cooling. This happens when one of the two SO$_4$ tetrahedra in each unit cell rotates by 108^0 about one of the three axes normal to the c-axis [5, 9, 11, 19]. On the other hand, Tomaszewski and Lukaszewics [31], using X-ray studies, proposed that the crystal transforms from hexagonal to another hexagonal phase with lower symmetry at 216 K, while in the temperature range between 164 K and 190 K the material shows
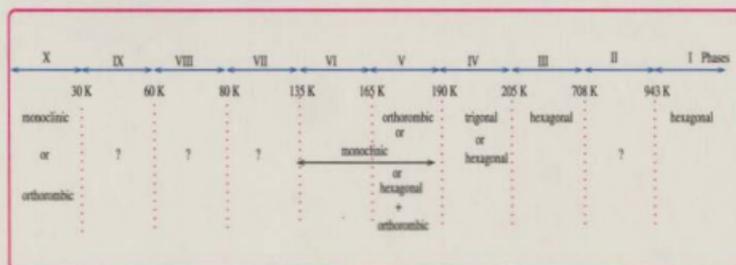
Figure 2.2: Sequence of phase structures for LiKSO$_4$ on cooling

a coexistence of hexagonal and orthorhombic phases. Moreover, the same authors reported [32] that the crystal structure transforms on cooling into an orthorhombic phase below 180 K, while the intermediate phase above this temperature is hexagonal. Other [37, 74] authors proposed that the crystal is monoclinic in the temperature range between 140 K and 190 K and trigonal in the temperature range between 190 K and 240 K.

In addition, definite results concerning the existence of phase transitions below 170 K and the symmetries of the different structures are still lacking [80]. At lower temperatures LiKSO$_4$ undergoes at least four or five phase transitions based on the results of the different techniques used so far; the symmetry of these phases is suggested but not clearly demonstrated [10, 48, 53, 80]. Also, there is some disagreement about the transition temperatures: Diosa et al. [22] stated that the transition temperatures are 38 K and 57 K on cooling using ac calorimetry, but their results from dielectric measurements show only one transition at 57 K on heating. A Raman spectroscopic study of LiKSO$_4$ by Liu et al. [80] showed that a transition occurs at 45 K. An Infrared spectroscopic study by Zhang et al. [74] showed transitions at 35 K, 60 K and 140 K on heating, while the same method used by Oliveira et al. [10] showed

only one transition at 30 K on heating.

Therefore, based on results obtained in the temperature range between 4 K and 300 K, there are different schemes proposed to describe the transitions in that temperature range. Liu et al. [80] summarized these results in the following diagram:

hexagonal $\rightleftharpoons^{210K}_{253K}$ trigonal $\rightleftharpoons^{172K}_{190K}$ orthorhombic or monoclinic $\rightleftharpoons^{20K}_{30K}$ unknown.
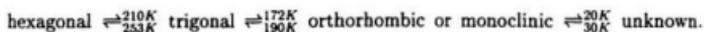
Whereas, Bhakay-Tamhane et al. [43] proposed another diagram:

(hexagonal) $\rightleftharpoons^{205K}_{250K}$ (trigonal) $\rightleftharpoons^{189K}_{190K}$ (unknown) $\rightleftharpoons^{135K}_{138K}$ (unknown).
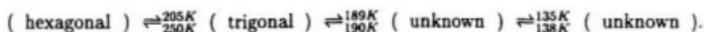
Depending on the results in the references [10, 14, 27, 37, 43, 44, 46. 47. 56, 59, 67. 68. 81], LiKSO$_4$ undergoes reconstructive phase transitions with decreasing temperature. LiKSO$_4$ crystal at room temperature is hexagonal and transforms to a trigonal phase at ∼ 205 K on cooling. Then at ∼ 190 K it transforms to monoclinic. There are also phase transitions at temperatures of 165 K, 135 K, 80 K, 60 K and 30 K, but the crystal structure of these low temperature phases is not yet known. However, a monoclinic structure was suggested by [22, 28] below 30 K. Moreover, we will refer to notation adopted in [37, 67], which is schematically summarized in Fig. 2.2.

2.2.2 Crystal Characteristics

The physical properties of LiKSO$_4$ can be summarized based on the results of previous work as follows:

1-Elastic Properties: The LiKSO$_4$ crystal is ferroelastic below 190 K (on cooling) based on the following results. Fujimoto et al. [25] have reported that the phase below 200 K and in the range between 200 K and 250 K (on heating) is ferroelastic based on the measurement of polarization and electric field. A. Ran Lim et al. [53] have shown that the LiKSO$_4$ single crystal undergoes a ferroelastic phase transition near temperature of 190 K. Also, Mroz et al. [52, 82] and Krajewski et al. [54] have

shown that the low temperature phase below 190 K is ferroelastic from the stress-strain hysteresis curve, using the torsion vibration technique. Neutron diffraction study proved that the phases in the temperature between 38 K and 240 K are ferroelastic, and this is confirmed by the splitting of the diffraction peaks, related to the domain structure [46]. Sorge and Hempel [59] showed that $LiKSO_4$ crystal is ferroelastic in the range between 150 K and 190 K using the optical investigations. N. K. Madi et al. [58] proved that ferroelasticity in $LiKSO_4$ crystal is an isotropic feature, depending on the response of the crystal to the radiation in different directions [58]. Breczewski T. et al. [23] proved that elastic properties of $LiKSO_4$ crystals vary nonlinearly in the 100w -300 K range.

2- Electrical Properties: Ando [7] has shown that $LiKSO_4$ does not exhibit a typical ferroelectric hysteresis curve. Also, the crystal is polar but not ferroelectric below 708 K based on the result of his pyroelectric experiment. Breczewski et al. [23] proved that the piezoelectric properties of $LiKSO_4$ crystals varies nonlinearly in the temperature range between 100 K and 300 K. J.E. Diosa et al. [22] proved that dielectric constants show two anomalies at cooling, while Oliveira et al. [10], relying on the dielectric constant and dielectric observations, showed that the transition which occurs at 253 K is first order with a large thermal hysteresis. The dielectric constant shows a strong temperature dependence below the transition temperature due to the motion of the domain walls as the temperature is varied. In any case, all phases at and below room temperature are pyroelectric [7, 23].

3- Commensurate & Incommensurate: F. Holuj et al. [61] and C. H. A. Fonseca et al. [62] suggested, based on an EPR study, that $LiKSO_4$ has an incommensurate phase in a region between approximately 183 K and 253 K on heating. On the contrary, P. E. Tomazewski et al. [31,32] based on X-ray study, showed that there is no incommensurate structure. Moreover, Sandhya Bhakay-Tamhane et al.

[44] did not find any evidence for the existence of an incommensurate phase in the temperature range 190-295 K by neutron study.

4- Thermal Properties: J.E. Diosa et al. [22] observed that specific heat anomalies at 38 K, 57 K, and 206 K. Sharma [6] using Fizeau's interferometer observed a major anomaly around 178 K in the linear thermal expansion coefficients α_a and α_c along the x and z directions.

5- Optical Properties: There have been many optical studies performed on LiKSO$_4$. Leitao et al. [57] measured the dependence of the birefringence on the applied uniaxial pressure and the related piezo-optic coefficients. The effects of uniaxial mechanical stresses σ_x and σ_y on the temperature (77-300 K) and spectral (25-880 nm) changes of the birefringence were studied in LiKSO$_4$ crystals by Stadnik et al. [83].

2.3 Acoustic Studies of the Phase Transitions and the Elastic Constants

One of the most useful techniques for investigating the elastic properties and phase transitions of crystals is the pulse echo method [84-87]. This technique is used to study phase transitions at high and low temperatures with and without exerted pressure on the sample. In addition to that, measurements of both compressional (longitudinal) and shear (transverse) waves in a solid enables the elastic constants to be obtained.

H. Kabelka and G. Kuchler [68] measured the elastic stiffness constants C_{11}, C_{33}, C_{44}, and C_{66} of LiKSO$_4$ in the temperature range 190-300 K by the ultrasonic pulse echo overlap method. The sample temperature was changed at a rate of 0.05 K/min on

cooling and 0.3 K/min on heating for C_{11} measurements. The transition temperature was found to be 207 ± 2 K on cooling and 244 ± 2 K on heating. In addition to that, they showed that the cooling/heating rate has an effect on the value of the transition temperature. Willis and Leisure [5] measured the complete set of the elastic constants for LiKSO$_4$ in the range between 200 K and 300 K. They observed an 80 % reduction of C_{66} at 213 K (on cooling) using resonant ultrasound spectroscopy. They also showed that all the elastic constants exhibit large step changes at 213 K except C_{13}. Moreover, they observed an increase of about 10% in C_{11} and C_{33} at the transition from the room temperature phase to the lower temperature phase. An et al. [21] observed a decrease of about the same magnitude. Borisov et al. [71, 72] studied the low temperature phase transitions in the LiKSO$_4$ crystal by a pulse acoustic technique at a frequency of 5 MHz under a slow cooling and warming rate of 0.2 K/min. They observed two transitions: the first around 204 K and the second around 185 K on cooling. On heating, the phase transition temperatures shifted to higher temperatures by about 60 K and 10 K, respectively.

Chapter 3

Theory

In this chapter, we will discuss crystalline elasticity, the propagation of plane wave in crystals, the solution of the Christoffel equation, Landau theory and its relation with the phase transition, and finally, structural phases.

3.1   Crystalline Elasticity

Under the action of applied forces, materials are generally deformed to some extent. It is often the case that the body returns to its initial undeformed state when the applied forces are removed. Such a deformation is called elastic. In the theory of elasticity we treat the solid body as a continuum; this approximation ignores the discreteness of any material made up of atoms, and it is valid for length scales large relative to the atomic dimensions. If the position of any point in the body before the deformation is defined by its position vector $\vec{R}$ (with components X_l where $l=1,2,3$), when the body is deformed, its new position vector will be $\vec{R}'$ (with components X_l'). Every point has a displacement vector $\vec{U}_i$ (X_l) $i, l = 1,2,3$. In this case, the

deformation may be described by a strain tensor of the second rank

$$S_{kl} = \frac{1}{2} \left[\frac{\partial U_k}{\partial X_l} + \frac{\partial U_l}{\partial X_k} + \sum_i \frac{\partial U_i}{\partial X_k} \frac{\partial U_i}{\partial X_l} \right] \tag{3.1}$$

For small strains, terms of the second order are neglected [88]. Therfore, this strain tensor reduces to

$$S_{kl} = \frac{1}{2} \left[\frac{\partial U_k}{\partial X_l} + \frac{\partial U_l}{\partial X_k} \right]. \tag{3.2}$$

The diagonal elements of S_{kk} (i.e., compressional or tensional strains) are a measure of the extension per unit length of the kth axis, while the off-diagonal elements ($k \neq l$) are a measure of the change of the angle between the k, l axes (i.e., shear strains).

The forces related to the deformation are described in terms of a stress tensor of the second rank T_{ij}, where i denotes the ith component of a force acting on a unit area, with normal along the jth axis, as illustrated in Fig. 3.1. The units of
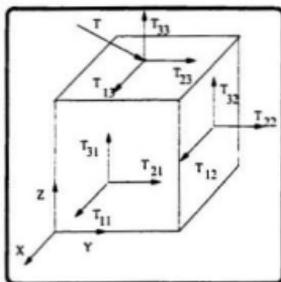
Figure 3.1: Stress Tensor Components

the stress components are force per unit area, and the number of independent stress components is reduced from nine to six by applying to an elementary cube (as in Fig. 3.2) the condition that the angular acceleration vanishes, and hence the total torque is zero. This gives $T_{ij} = T_{ji}$ in the absence of body torques [89]. The stress
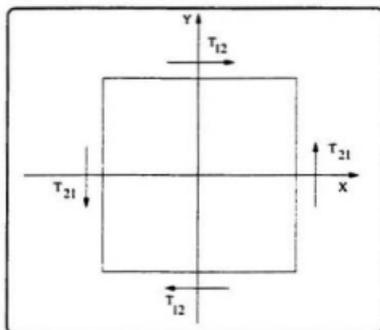
Figure 3.2: For a body in static equilibrium $T_{12} = T_{21}$. The sum of the forces in the x and y directions is zero. Therefore the total force is equal to zero, hence the total torque about the origin is also zero.

components for which $i = j$ (the diagonal components) are the normal components of stress, and those for which $i \neq j$ are the shear stress (off-diagonal components). The stress and strain tensors can be represented by the following arrays: the stress tensor is

$$T_{ij} = \begin{bmatrix} T_{11} & T_{12} & T_{13} \\ T_{21} & T_{22} & T_{23} \\ T_{31} & T_{32} & T_{33} \end{bmatrix}, \tag{3.3}$$

while the strain tensor is

$$S_{ij} = \begin{bmatrix} S_{11} & \frac{1}{2}[S_{12} + S_{21}] & \frac{1}{2}[S_{13} + S_{31}] \\ \frac{1}{2}[S_{12} + S_{21}] & S_{22} & \frac{1}{2}[S_{23} + S_{32}] \\ \frac{1}{2}[S_{13} + S_{31}] & \frac{1}{2}[S_{23} + S_{32}] & S_{33} \end{bmatrix}. \tag{3.4}$$

For linear elasticity, the strain tensor S_{kl} is proportional to the stress tensor T_{ij} and

Tensor	11	22	33	23 or 32	13 or 31	12 or 21
Matrix	1	2	3	4	5	6

Table 3.1: Conversion from tensor to the matrix notation

a generalized Hooke's law[1] holds so that

$$S_{kl} = \sum \varepsilon_{ijkl} \cdot T_{ij}, \tag{3.5}$$

$$T_{ij} = \sum C_{ijkl} \cdot S_{kl}, \tag{3.6}$$

where the C_{ijkl} are the elastic stiffness constants, and ε_{ijkl} is the inverse of C_{ijkl}, called the elastic compliance. Both of them are tensors of the 4th rank, and the value of C_{ijkl} depends on the direction within the material (anisotropic). In order to write the fourth rank tensor with two subscripts, conversion from tensor to the matrix notation is necessary, which is summarized in Table 3.1. This conversion gives

$$T_\alpha = \sum C_{\alpha\beta} . S_\beta \tag{3.7}$$

where α and $\beta = 1, 2, 3, 4, 5, 6$. It appears that there are 81 (3^4) independent elastic constants. This number is decreased to 36 in the absence of body torques[2], since $T_{ij} = T_{ji}$. Due to the symmetry of $C_{ijkl} = C_{klij}$ (which is a result of the condition that the strain energy be a function only of the state of the material), the number of independent elastic constants is decreased to 21. This number is further decreased due to the symmetry of the crystals. The higher the crystal symmetry, the fewer the number of independent terms that exist in the matrix. For example, a single crystal with hexagonal symmetry has only five independent elastic constants and a cubic

---

[1] Hooke's law states that in an elastic medium for sufficiently small deformations the strain is proportional to the stress

[2] Forces are divided into body forces and surface forces: the body force magnitude is proportional to the volume, while the surface force magnitude is proportional to the surface area enclosing the volume

crystal has only three independent elastic constants [90, 91]. The elastic constant matrix for a hexagonal crystal is given by the following equation

$$
C_{ij} = \begin{bmatrix}
C_{11} & C_{12} & C_{13} & 0 & 0 & 0 \\
C_{12} & C_{11} & C_{13} & 0 & 0 & 0 \\
C_{13} & C_{13} & C_{33} & 0 & 0 & 0 \\
0 & 0 & 0 & C_{44} & 0 & 0 \\
0 & 0 & 0 & 0 & C_{44} & 0 \\
0 & 0 & 0 & 0 & 0 & C_{66}
\end{bmatrix},
\tag{3.8}
$$

where $C_{66} = (C_{11} - C_{12})/2$

3.2   Plane Wave Propagation

Two kinds of elastic waves can propagate in solids: longitudinal and transverse. The polarization is parallel/normal to the wave vector K in a longitudinal/transverse wave, respectively. Since solids can sustain shearing strains elastically, they will support the propagation of both types of wave. In the general case, three modes can propagate in a given direction in a crystal: a quasi-longitudinal wave and two quasi-transverse waves. The polarizations of these three waves are always mutually orthogonal. The rate at which a stress-induced strain propagates through an elastic medium when a force is applied to it is given by Newton's second law and Hooke's law. Newton's second law gives the general equation of motion for an elastic medium

$$
\frac{\partial T_{ij}}{\partial X_j} = \rho \frac{\partial^2 U_i}{\partial t^2},
\tag{3.9}
$$

where ρ is the mass density and body forces are neglected. The net force is due to the spatial variation of the stress. Combining Eqs. 3.1, 3.5 and 3.9 and using the

symmetry $C_{ijkl} = C_{ijlk}$ gives the equation of motion

$$C_{ijkl} \frac{\partial^2 U_k}{\partial X_j \partial X_l} = \rho \frac{\partial^2 U_i}{\partial t^2}. \tag{3.10}$$

Its solution is a plane monochromatic wave

$$U_i = u_i e^{i(K_\alpha X_\alpha - \omega t)} \tag{3.11}$$

where ω is the frequency, K is the wave vector and u_i are the amplitudes satisfying

the conditions

$$[C_{ijkl} K_j K_l - \rho \omega^2 \delta_{ik}] U_k = 0. \tag{3.12}$$

Dividing equation 3.12 by K^2, it takes the form

$$[\lambda_{ik} - \rho \nu^2 \delta_{ik}] U_k = 0, \tag{3.13}$$

where $\nu = \omega/K$ is the phase velocity or the acoustic velocity, and

$$\lambda_{ik} = \frac{[C_{ijkl} K_j K_l]}{K^2} = C_{ijkl} n_j n_l \tag{3.14}$$

is the Christoffel matrix, which gives λ_{ik} in terms of the elastic constants. Here n_i

is the direction cosine of the wave normal with respect to the axes x, y, z Fig. 3.3.

To find the solution, the determinant of the secular equation is set equal to zero as

shown in:

$$|\lambda_{ik} - \rho \nu^2 \delta_{ik}| = 0. \tag{3.15}$$

The values of n_i for different directions are given in Table 3.2. The result of solving

the secular equation for a hexagonal crystal for different crystal directions for different

modes is given in Table 3.3. The solutions relate the acoustic velocity of the elastic

waves to a set of independent elastic constants that characterize the elastic properties

of the material. Thus, the elastic properties of the sample can be calculated from

velocity measurements that can be obtained accurately.
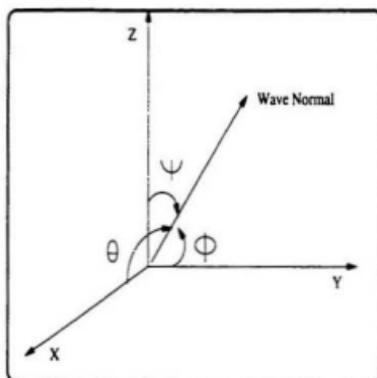
Figure 3.3: The direction cosines of the wave vector $n_1 = \cos\theta$, $n_2 = \cos o$ and $n_3 = \cos v$.

Direction	n_1	n_2	n_3
[100]	1	0	0
[010]	0	1	0
[001]	0	0	1

Table 3.2: The values of the n_i for different directions

3.3 Phase Transitions and Landau Theory

A phase is a homogeneous part of a given assembly of atoms or molecules, which can be described by thermodynamic properties like volume V, pressure P, temperature T and free energy G. When the Gibbs free energy G is minimum the phase will be stable under specified thermodynamic conditions. As the variables acting on a system are varied the free energy of the system changes. Whenever such variations of free energy are associated with changes in structural details of the phase, a phase transition is

Direction	Mode	$\rho \nu^2$
..	L	C_{11}
[100]	T_z	C_{44}
..	T_y	C_{66}
..	L	C_{11}
[010]	T_z	C_{44}
..	T_x	C_{66}
..	L	C_{33}
[001]	T_x	C_{44}
..	T_y	C_{44}
..	L	$\frac{1}{4}[C_{11} + C_{33} + 2C_{44} + \sqrt{(C_{11} - C_{33})^2 + (2C_{44} - 2C_{13})^2}]$
[101]	$T_{[010]}$	$\frac{1}{4}[C_{11} + C_{33} + 2C_{44} - \sqrt{(C_{11} - C_{33})^2 + (2C_{44} - 2C_{13})^2}]$
..	$T_{[\bar{1}01]}$	$\frac{1}{2}[C_{66} + C_{44}]$

Table 3.3: Solutions for three wave vectors in hexagonal crystals. where L is longitudinal, T_j is transverse wave with polarization along the jth axis.

said to occur [92].

Landau free energy theory is a thermodynamic theory which is used extensively to describe phase transitions without giving any information about the microscopic causes of the transition. It is based on the idea of an order parameter Q, where the free energy G is expanded in a power series of the order parameter Q [93].

3.3.1 Order Parameter Q

The concept of an order parameter provides a very general way of examining phase transitions. An order parameter Q measures the extent of the departure of the atomic

configuration in the less symmetric phase from that in the more symmetric phase (i.e., it is assumed to be some quantity that differentiates the two phases involved). The high symmetry phase possesses all the symmetry elements of the low symmetry phase, plus one or more additional symmetry elements. As long as Q takes on a value of zero, the crystal symmetry is that of the high symmetry phase. As soon as Q takes on any arbitrarily small value, the symmetry is reduced to that of the low symmetry phase [5][3]. For example, any physically observable quantity which varies with temperature can be taken as an experimental order parameter. Hence, the rotation of SO_4 tetrahedra in the unit cell of $LiKSO_4$ crystal can be taken to be an order parameter [5].

3.3.2 Phase Transition Order

Phase transitions are classified as first, second, or higher order. Many real transformations are truly of mixed order, exhibiting features of both first and second order. Continuous transitions are known as second order phase transitions, while, first order phase transition occurs when the order parameter jumps discontinuously. In general, a transition is said to be of the same order as the derivative of the Gibbs free energy which shows a discontinuous change at the transition. We know that the Gibbs free energy is given by

$$dG = V dP - S dT \qquad (3.16)$$

so the first derivatives of the free energy are the volume

$$V = \left(\frac{\partial G}{\partial P}\right)_T \qquad (3.17)$$

---

[3]The order parameter Q = 0 for $T > T_c$, higher symmetry phase, and (Q ≠ 0) for $T_c > T$, low symmetry phase [93].

and the entropy

$$S = -(\frac{\partial G}{\partial T})_P. \tag{3.18}$$

The second derivatives of the free energy are

$$-\frac{C_P}{T} = (\frac{\partial^2 G}{\partial T^2})_P \tag{3.19}$$

and

$$V\alpha = \frac{\partial^2 G}{\partial P \partial T} \tag{3.20}$$

where C_P is the heat capacity and α is the thermal expansion coefficient. Therefore. a transformation in which a discontinuous change occurs in volume V and entropy S belongs to the first order (that is. when there is a latent heat of transformation). and those in which a discontinuous change occurs in C_P and α belong to the second order.

Chapter 4

Experimental Setup

4.1 Sound Velocity Measurement

4.1.1 The Standard Pulse-Echo Method

In this section, we will describe how the absolute sound velocity can be measured in single crystals. We first present what is known as the standard pulse-echo method. In this standard approach, illustrated in Fig. 4.1, a transducer is glued to one of the two opposite parallel faces of the sample under investigation. The transducer is simply a solid state device that is used to convert a pulsed radio frequency signal into a mechanical vibration at the same frequency, owing to the piezoelectric effect. The configuration of the ultrasonic transducers used in our experiment consists of two electrodes plated on opposite faces of a thin piezoelectric crystal. As the transducer is mechanically bonded to the crystal, the vibration of the crystal's face generates a sound wave which propagates through the sample, and every time it reaches one of the sample's extremities it gets reflected. Consequently, each time the acoustic wave returns to the transducer, a small fraction of the wave's energy is converted into an
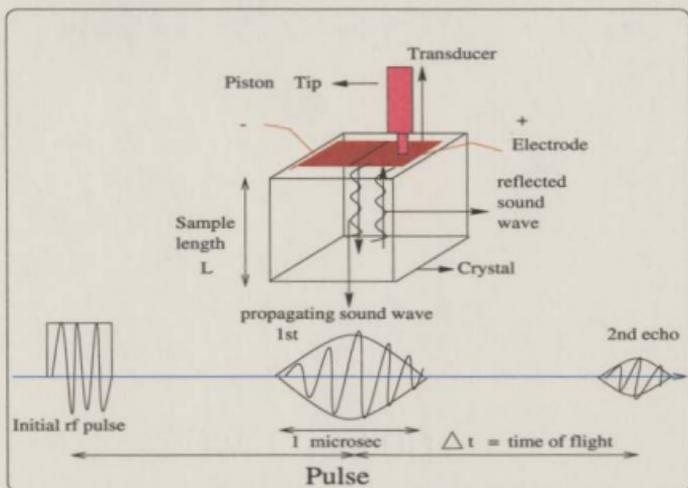
Figure 4.1: The reflection configuration and consecutive echoes

electrical signal (inverse piezoelectric effect). Thus, if the acoustic attenuation is not too large, a multi-echo pattern can be directly observed on an oscilloscope, as shown in Fig. 4.1. In this case, the absolute sound velocity can be simply determined by measuring the time of flight between two consecutive echoes Δt. In the reflection configuration, considering that the time Δt corresponds to the time needed for the sound wave to travel from one end and to return, the velocity can be calculated using

$$v = \frac{2L}{\Delta t} \tag{4.1}$$

where L is the sample length in the direction of propagation [94–96].

In general, the typical length of samples used in these experiments is between 3 and 10 mm. Considering that the sound velocity in solids ranges between 3000 m/s and 8000 m/s, the time for the sound wave to travel from one end and to return

is between 1 μs and 7 μs. Based on the uncertainty on the time of flight and the sample's length determination, the relative uncertainty on the velocity measurement

$$\frac{\delta v}{v} = \sqrt{\left(\frac{\delta(\Delta t)}{\Delta t}\right)^2 + \left(\frac{\delta L}{L}\right)^2}. \qquad (4.2)$$

is approximately 0.1%, under good conditions. Thus, if one wants to investigate phase transitions using the absolute sound velocity measurement, an accuracy of 0.1% is generally not good enough. Practically, measurements with a better accuracy can be obtained by using a longer sample. However, the increment of the sample's length is limited due to the finite space in the sample holder and the crystal's attenuation. Even with this improvement, the accuracy would still be of the order of 0.05%. Consequently, we need another approach with high accuracy to observe phase transitions. This can be achieved by measuring the relative change in velocity, where the resolution can be as high as few parts per million, as we will see in the coming section.

4.2   The Acoustic Interferometer

The principal disadvantage of the standard pulse-echo method lies in its low resolution. We will now show how it is possible to achieve resolution as high as 1 part per million (ppm) using an experimental technique that measures the relative change in sound velocity $\Delta v/v$ instead of the absolute velocity.

The relative change in sound velocity measurements are realized using an acoustic interferometer. We will now discuss its principle of operation based on the acoustic interferometer schematic pictured in Fig. 4.2. As shown in this figure, a continuous radio frequency signal (cw rf) of frequency f, generated by a frequency synthesizer [6061A Synthesized RF Generator, 10 KHz-1050 MHz, Giga-tronics] is divided by a power splitter into two parts. The signal that we call "the reference signal" is used
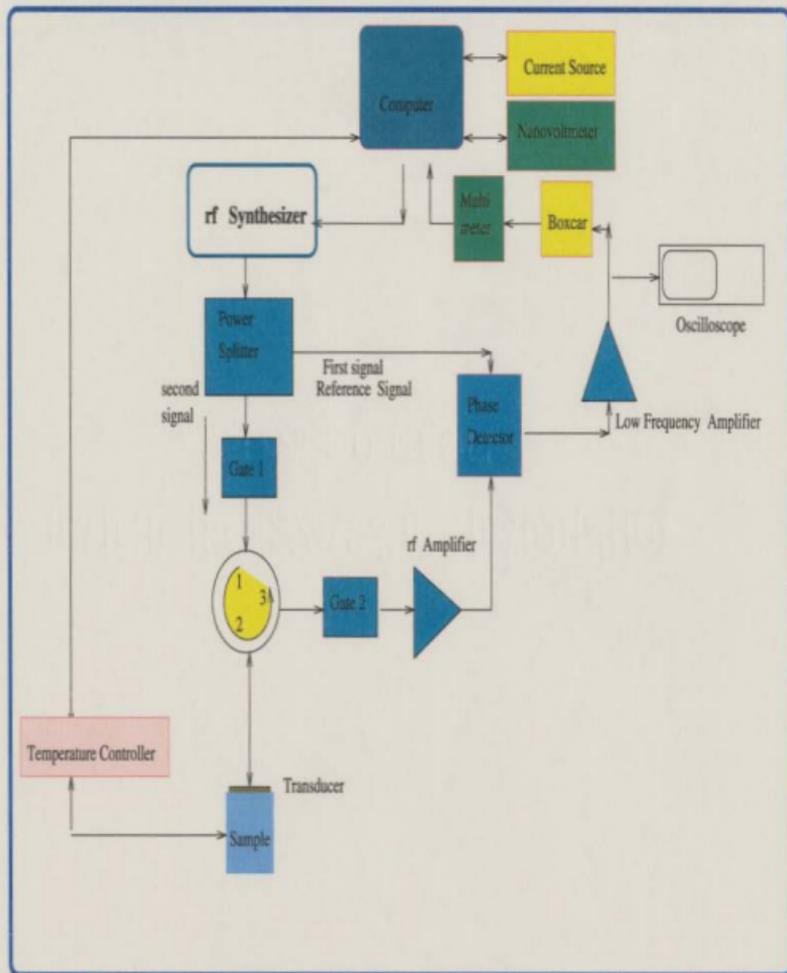
Figure 4.2: Block diagram of the acoustic interferometer

subsequently for a phase comparison with the signal coming back from the sample. The second half of the signal is passed through a gate (gate one) that shapes it in a series of short pulses of about 1 μs at a repetition rate of 1000 pulses per second. The pulse signal enters a circulator at point one and leaves at point two, where it excites a transducer bonded on the sample. The main purpose of the circulator is to protect the frequency synthesizer from any reflected signals from the transducer. As described in section 4.1.1, the transducer converts the rf electrical signal into a mechanical vibration that generates a sound wave which propagates through the sample. As the wave reaches the sample's extremity, it gets reflected back toward the transducer. Every time the wave reaches the transducer again, a small fraction of that signal is converted into an electrical signal. Then, this rf multi-echo signal passes through the circulator at position two and exits at three. The purpose of the second gate is to cut off the initial pulse from the echo pattern in order to prevent saturation of the amplifier placed after the second gate. The reference signal and the rf echo signal are then compared, and a new signal proportional to their phase difference is obtained at the phase detector output. A typical output of the phase detector, which gets displayed on an oscilloscope, is shown in Fig. 4.3. In this particular case, we notice that the signal is positive for the first, third and fourth echo. However, for the second echo the signal is negative. As this signal represents the relative phase between the echo and the reference signal, the signal displayed in Fig. 4.3 illustrates a case where the first and third echoes are in phase with the reference signal (or a multiple of 2π) while the second echo is out of phase. Fig. 4.3 also illustrates that the amplitude of the echo decreases as the time of flight increases. This is a result of the attenuation of the wave as it propagates in the crystal.

During an experiment, the amplitude of one particular echo, normally the first one, is measured using a box car averager. That measurement is in fact a reading
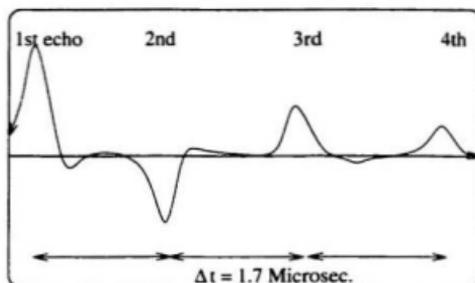
Figure 4.3: Snapshot of echoes for a sample of length 4.2 mm

of the phase difference between that particular echo and the reference signal. In the case of the nth echo, considering that the phase difference Φ_n is proportional to the time of flight Δt_n, we must have

$$\Phi_n = 2\pi f \Delta t_n \qquad (4.3)$$

where f is the frequency of the sound wave which is also the frequency of the rf signal. Knowing that the velocity of the acoustic wave is simply given by the time of flight divided by the distance traveled, we must have

$$v = \frac{\Delta t_n}{2Ln} \qquad (4.4)$$

where L is the sample's length. Combining this last equation with equation (4.3), we obtain an expression for the relative phase of the nth echo Φ_n which is given by

$$\Phi_n = \frac{4\pi n L f}{v}. \qquad (4.5)$$

From this last expression, we derive the expression for the relative phase variation

$$\frac{\Delta \Phi_n}{\Phi_n} = \left(\frac{\Delta f}{f}\right) + \left(\frac{\Delta L}{L}\right) - \left(\frac{\Delta v}{v}\right). \qquad (4.6)$$

Consequently, we see that any phase variation, due to modification in external parameters (pressure (P), temperature (T), magnetic field (**B**)), can be compensated by adjusting the frequency. Therefore, by imposing a constant phase during the experiments ($\Delta\Phi = 0$), we see how the relative change in velocity $\Delta v/v$ can be related to the variation in the synthesizer frequency $\Delta f/f$ as well as the change in the sample's length $\Delta L/L$:

$$\frac{\Delta v}{v} \cong \left(\frac{\Delta f}{f}\right) + \left(\frac{\Delta L}{L}\right). \tag{4.7}$$

For measurements as a function of temperature, the variation of the sample's length can be easily estimated using the thermal expansion coefficient. Based on experimental values, it is common to obtain a variation in the relative change in sound velocity $\Delta v/v$ that is an order of magnitude larger than the change in the relative sample's length $\Delta L/L$. Hence, if we neglect the thermal expansion, we finally obtain that the relative change in sound velocity can be approximated by

$$\frac{\Delta v}{v} \cong \frac{\Delta f}{f}. \tag{4.8}$$

Therefore, every time the box car measures a change in the phase, the computer adjusts the frequency of the synthesizer in order to bring the phase back to its initial value. The frequency shift Δf, under this condition, is directly proportional to the variation of the relative change in sound velocity $\Delta v/v$. In this technique, the frequency stability of the synthesizer is really what ensures the high resolution of the interferometer. The frequency used in these experiments is normally around 30 MHz with the possibility of changing it in steps as small as 10 Hz. Hence, a resolution of 0.3 ppm could, in principle, be achieved using this approach.

4.3   The Pressure Cell and the Sample Holder

One of the goals of this project is to measure the temperature phase diagram of lithium potassium sulphate below room temperature. This can be achieved by measuring the temperature dependence of the sound velocity in single crystals. Initially, in order to perform these measurements, we simply glued the transducer on the $LiKSO_4$ crystal using a thin layer of silicone (adhesive sealant). However, all our attempts to cool down samples below 200 K failed whenever the transducer was glued to the crystal's surface. As the samples cool down, we generally lose the signal due to the deterioration of the thin film of adhesive between the transducer and the crystal. We believe that this is induced by the change in the lattice parameters of $LiKSO_4$ at 195 K and 185 K. According to measurements realized by Tomaszewski and Lukaszewicz [32] and Desert et al. [37], the lattice parameter along the c-axis and a-axis changes by 0.3 % and 0.6 %, respectively. Consequently, because of that large thermal contraction at the phase transitions, it is not surprising that a large stress builds up within the glue and that is why we eventually lose the coupling between the transducer and the sample with further cooling. Therefore, in order to obtain reproducible results, we decided to use a liquid instead of a glue as the transmitting medium between the transducer and the sample. After trying many liquids with different freezing temperatures, we finally chose to use a 3methyl-1-butanol solution which has a freezing temperature of 123 K at ambient pressure. Because of its low freezing temperature, the thin film between the transducer and the sample is still fluid as we cool down the samples below the thermal contraction observed in $LiKSO_4$. Consequently, no stress can develop within the sample-transducer interface. However, 3methyl-1-butanol is highly volatile. Consequently, if no special precautions are taken, we eventually lose the sample-transducer coupling after a while. To address this problem, we chose to put

the sample-transducer assembly into a sealed Teflon capsule filled with the same 3methyl-1-butanol solution. As this is also how we normally mount samples for work under hydrostatic pressure, we decided to use the pressure cell even for measurements at ambient pressure. Using this approach, we finally obtained reproducible results on LiSO$_4$ in the temperature range from 80 K to 300 K at ambient pressure. The same system was also used for measurements at higher pressures.

A description of the pressure cell and its principle of operation will be presented here using the diagram shown in Fig. 4.4. The pressure cell assembly is composed of a hollow cylinder, a piston (plug), a Teflon cell filled with an incompressible liquid, an obturator with electrical leads and two screws to lock the different parts tight together. Inside the Teflon cell we also have the sample and a thin wire of lead used to measure the pressure [97]. The hydraulic pressure on the sample was exerted using a hydraulic unit. A force on the pusher was applied using the hydraulic unit. As a result, the piston (plug) moves and generates a pressure as the Teflon cell and the pressure medium (the liquid) are compressed. At the desired pressure, the screw behind the piston was firmly tightened to lock the piston in place so that the pressure cell could be removed from the hydraulic press. To increase the pressure on the sample, more force was applied on the pusher, and the cap was tightened again as seen in Fig. 4.4. Due to the liquid inside the cell (the pressure medium), equal pressure is applied to the different directions in the Teflon cell. To withstand large mechanical pressures, up to 12 kbar, the pressure cell is constructed of a copper-beryllium alloy (Cu-Be).

Since the transducer could not be glued to the sample for these measurements, we had to design a special sample holder shown in Fig. 4.5. The sample holder is made of copper, and it has two circular bases at its ends. The bottom one supports the sample, while a small spring-loaded piston is mounted in the upper one. The latter is composed of a hollow cylinder, a tip with small diameter (less than 1 mm) and a

Electrical leads

A

Liquid
Piston tip
Sample

16 cm

9.5   mm
30   mm

B

Screw

Obturator

Teflon cap
Sample holder
Transducer
Body of the pressure cell
(Cu-Be)

Piston (Plug)

Cylinder

Cap (screw)
Pusher
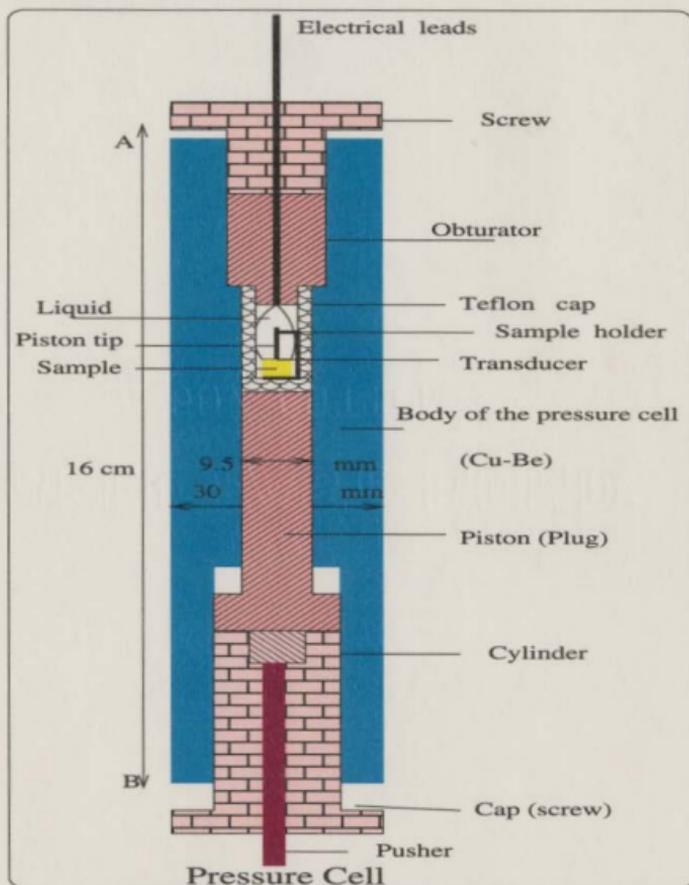
Pressure Cell

Figure 4.4: The pressure cell components
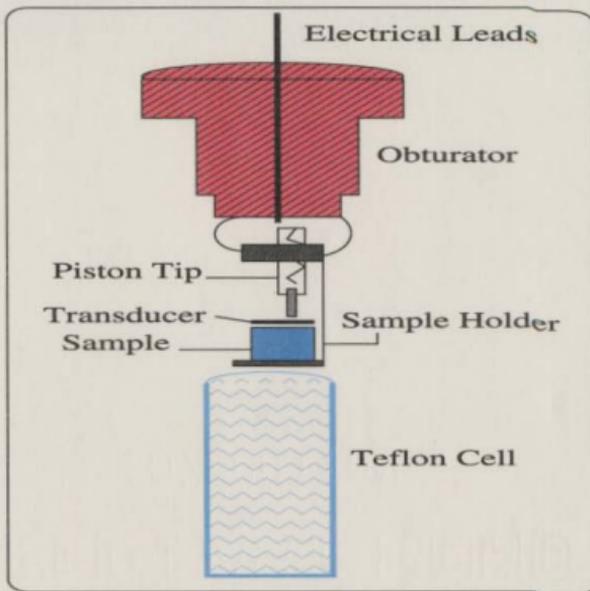
Figure 4.5: The sample holder and the Piston Tip

spring. The piston tip is movable in order to maintain the transducer on the sample.

Now, we will present the procedure of mounting the sample. The sample was placed in the sample holder with a drop of 3methyl-1-butanol on its upper surface. The piston tip was then adjusted so that it gently presses the transducer on the sample surface. The obturator bearing the sample holder was placed in the Teflon cell, which was filled with the same 3methyl-1-butanol solution. The obturator was then introduced into the bore of the pressure cell with a small force. Finally, the pressure cell was closed by two screws.

4.4   Pressure and Temperature Measurements

The pressure cell was also used to study the effect of pressure on the sound velocity and the phase transitions of $LiKSO_4$. In order to determine the pressure at room temperature, the resistance of a thin wire of lead (Pb) was measured in a four point contact configuration. As mentioned previously, this wire was inside the Teflon cell filled with a 3methyl-1-butanol solution. The pressure was calculated using the pressure dependence of the normalized resistance $R(P)/R(0)$ of lead measured at room temperature. The data obtained by Witting et al [98] are reproduced here in Fig. 4.6. A 5th order power series was derived from these data and subsequently used in
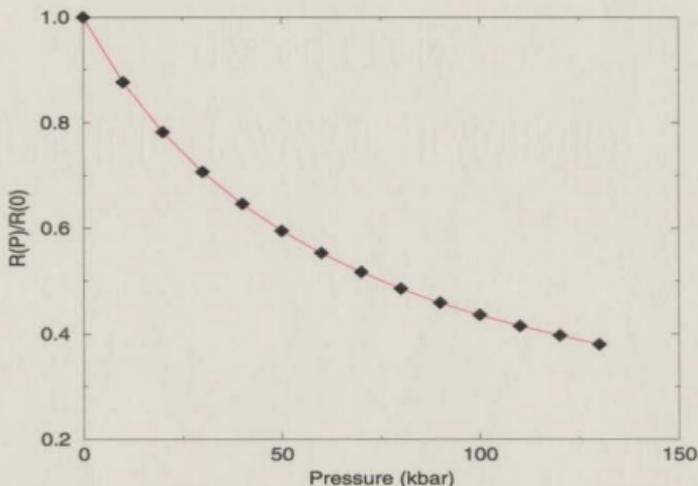
Figure 4.6: The ratio of the resistance of lead $R(P)/R(0)$ as a function of pressure, where $R(P)$ is the resistance of the lead wire as a function of pressure at room temperature and $R(0)$ is the resistance at ambient pressure and room temperature

our experiments to obtain the pressure. The expression for the power series is

$$P(R(P)/R(0)) = 946.375476 - 4839.81857 * x + 11168.9788 * x^2$$
$$-13719.2725 * x^3 + 8641.97037 * x^4 - 2198.23769 * x^5. (4.9)$$

where x = R(P)/R(0) is the normalized resistance measured at room temperature. In principle, this expression can be used to evaluate pressure up to 125 kbar.

It is well known that as you cool down clamp pressure cells, a pressure drop of a few kbar is often observed. The hydrostatic pressure inside the Teflon cell decreases with cooling, as a result of a different thermal contraction for the cell and the piston. Therefore, the effective force on the Teflon cell decreases. Consequently, there is a need for a suitable method to determine the pressure at different temperatures. For this reason, the temperature dependence of a lead wire resistance measured at ambient pressure R(0,T) and at pressure P, R(P,T), are compared in Fig. 4.7. In both cases, the temperature dependence can be approximated by a linear dependence

$$R(P, T) = m(P)T + R_0 \qquad (4.10)$$

for temperatures above 100 K. The slope m(P) is pressure dependent and R_0 is the y intercept equal to - 0.006 Ω which is almost a pressure independent. Therefore, if we neglect R_0, it is easy to show that the ratio R(P,T)/R(0,T) is also temperature independent

$$\frac{R(P,T)}{R(0,T)} = \frac{m(P)T + R_0}{m(0)T + R_0} \cong \frac{m(P)}{m(0)}. \qquad (4.11)$$

Thus, in order to evaluate the pressure, a quadratic fit was applied to the resistance curve measured at ambient pressure R(0,T). Subsequently, that fit was used to normalize the resistance R(P,T) measured at pressure P, as shown in Fig. 4.8. Considering that the pressure dependence of the normalized resistance R(P)/R(0)
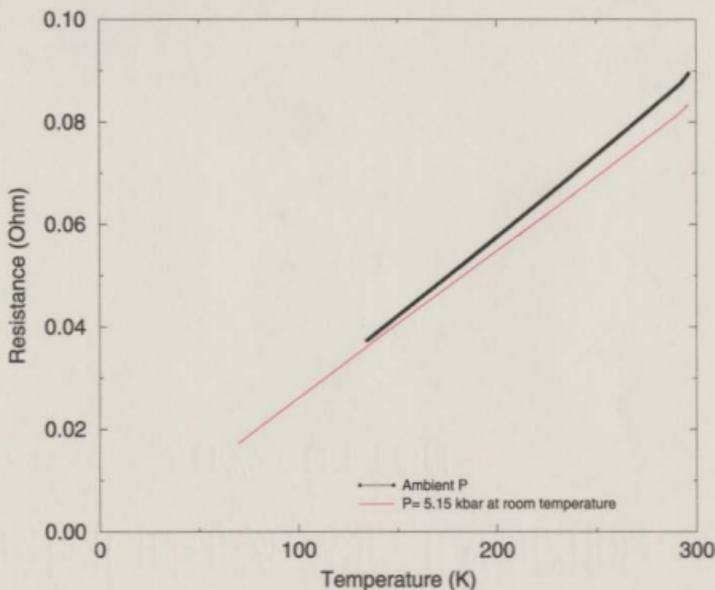
Figure 4.7: The resistance of lead as a function of temperature at two different pressures.

is temperature independent, the expression 4.9 was used to obtain the pressure as a function of the temperature, as shown in Fig. 4.9. From these curves, it is clear that the hydraulic pressure decreases with cooling until the freezing temperature of the liquid is reached then remains constant. The pressure was measured using this method to an accuracy of 0.1 kbar.

In order to measure the temperature of the sample, a calibrated sensor (Model CX-1050-SD, Lake Shore) was used. This sensor was in contact with the pressure cell, which can be considered as a heat reservoir for the sample. The temperature was
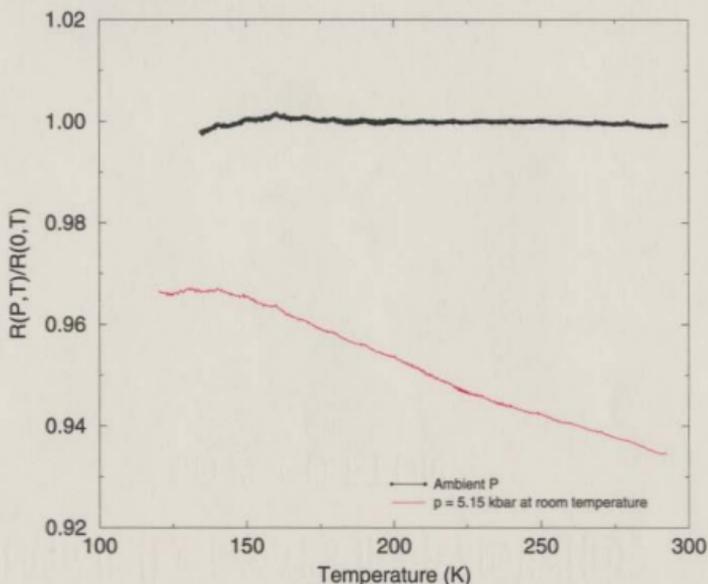
Figure 4.8: The ratio R(P,T)/R(0,T) as a function of temperature.

controlled via a Lake Shore 340 temperature controller. Temperature was measured in this method to an accuracy of 0.001 K.

4.5 Preparation of LiKSO$_4$ Samples

The lithium potassium sulphate crystals used in this study were grown at the crystal physics division of the Adam Mickiewicz University in Poznan (Poland). The crystals were obtained from an aqueous solution that contained an equimolar proportion of K$_2$SO$_4$ and Li$_2$SO$_4$. The crystals were grown under isothermal conditions at 315 K by slow evaporation. The crystal grew in a hexagonal shape with a clearly defined
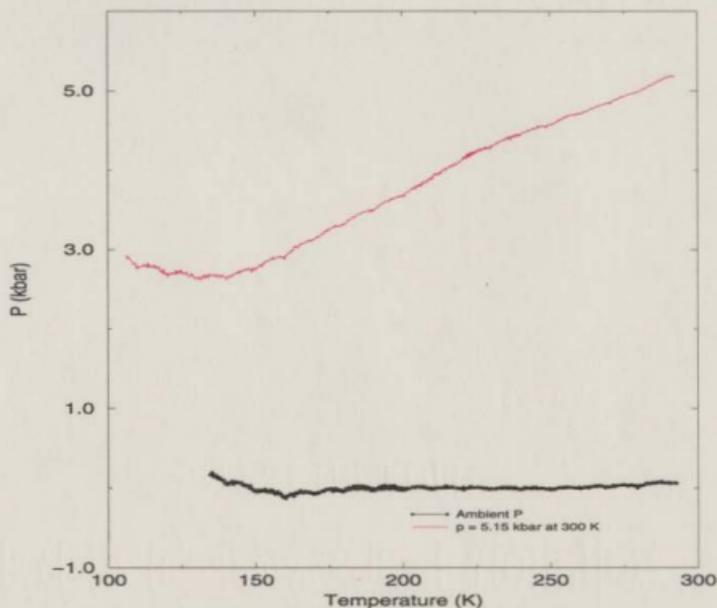
Figure 4.9: Pressure-Temperature Calibration Curve

six fold axis permitting an immediate identification of the z-axis.

For the purpose of this project, single crystals were cut so that we could measure the sound velocity of acoustic waves propagating along the x-axis [100] or z-axis [001]. The specimens were cut from untwinned parts of a large crystal using a wire saw[1] with a mixture of glycerine and silicon carbide with a 600 grain size number. The crystal's faces were then polished using silicon carbide. The initial stage was performed using a grain size number of 600 down to a grain size number of 1600. After all these operations, the sample dimensions were approximately 4mm×4mm×4mm

---

[1]South Bay Technology inc., model 850

to fit inside the Teflon cell. Furthermore, the symmetry axis of the samples can be confirmed using polarized light. The sample is placed between two polarizers with their optical axes rotated by 90°, as in Fig. 4.10. As the sample is rotated around its
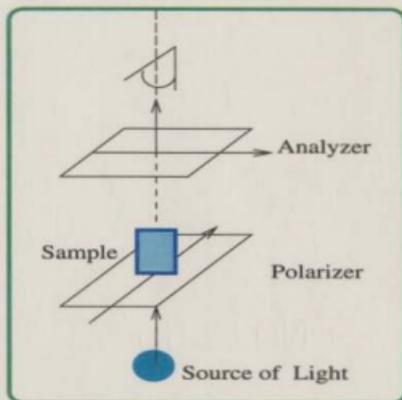
Figure 4.10: Procedure to confirm the z-axis

z-axis, no significant modification in the intensity of the transmitted light is observed. In this case, the axis of polarization of the electromagnetic wave remains parallel to the plane formed by the x and y axis of the crystal. As these two directions are equivalent in the hexagonal structure, no variations are expected as the crystal is rotated around its z-axis or c-axis. However, as the crystal is rotated around the x-axis, the axis of polarization of the electromagnetic wave rotates between the y-axis and z-axis which have very different optical activities. Consequently, if the crystal is rotated around the x-axis (or y-axis), a large change is observed in the intensity and color of the transmitted light every time the crystal is rotated by 90°. This method was used for all samples to confirm their orientation.

Chapter 5

Results

The effects of hydrostatic pressure and temperature on the sound velocity will be discussed in this chapter. First, the absolute sound velocities for transverse and longitudinal waves propagating along the x, y and z directions have been measured at room temperature. From these values, we could deduce the different elastic constants C_{ij} of LiKSO$_4$ for the hexagonal crystal structure. Secondly, the temperature dependence of the sound velocity measured at ambient pressure will be presented for longitudinal waves propagating along the x and z directions, respectively. Then, we will present the temperature dependence of the sound velocity obtained at different pressure for longitudinal modes propagating along the x-axis. From these results, we will derive the pressure-temperature phase diagram of LiKSO$_4$ for the temperature range between 4 K and 300 K. The various results obtained in this thesis will be discussed and compared with previous experimental studies.

5.1   Sound Velocity and the Elastic Constants

The absolute sound velocities for longitudinal and transverse waves propagating along
the x, y, and z directions have been measured at room temperature and ambient
pressure. They were determined by measuring the time of flight Δt between two
consecutive echoes for samples of length L. As described in section 4.1, the velocity
is then obtained using

$$v = \frac{2L}{\Delta t}. \tag{5.1}$$

The calculated values of the absolute sound velocity are listed in Table 5.1. Using

Direction	Mode	$v \pm \Delta$ v (m/s)
..	L	4900 ± 50
[100]	T_y	2430 ± 20
..	T_z	2900 ± 30
..	L	4920 ± 50
[010]	T_z	2900 ± 30
..	T_x	2430 ± 20
..	L	5300 ± 50
[001]	T_x	2970 ± 30
..	T_y	2970 ± 30

Table 5.1: Sound velocity in LiKSO$_4$ crystal in different directions in m/s, where L
is the longitudinal mode, T_j is transverse wave with polarization along the jth axis

these values and the density ρ of LiKSO$_4$ crystal measured at room temperature (ρ
= 2390 kg/m^3) [16, 21], the elastic stiffness constants associated with the different

propagating modes, are calculated by

$$v = \sqrt{\frac{C_{ij}}{\rho}} \qquad (5.2)$$

in accordance with table 3.3. The elastic stiffness constants are given in table 5.2 along with those obtained by other groups. The results published in references [68, 73] were obtained using an ultrasonic pulse echo overlap method while results contained in references [3, 16, 17, 19] were from Brillouin light scattering experiments. Our results are in good agreement with values reported by all these groups except for those obtained by Drozdowski et al. [17]. Moreover, their value for C_{66} is abnormally high and also very different from the value reported by all othwer groups.

$C_{ij} \backslash ref$	New Results	[73]	[3]	[68]	[16]	[19]	[17]
C_{11}	5.7±0.1	5.724±.006	5.67	5.50±0.11	5.69±0.06	5.74	5.16
C_{12}	2.92±0.06	2.866±.003	2.83±0.15	2.64±0.14		2.92	
C_{13}		2.237±.002	2.35		2.65		
C_{33}	6.7±0.1	6.735±.007	6.71±0.08	6.53±0.13	6.67±0.07	6.73	5.23
C_{44}	2.11±0.04	2.151±.002	2.14	2.05±0.04	1.86	2.11	
C_{66}	1.41±0.03	1.429±.001	1.42±0.05	1.43±0.03	2.00	1.42	5.70

Table 5.2: Elastic constants in 10^{10} N/m^2 of LiKSO$_4$ in comparison with previous measurements, where C_{11} - 2 $C_{66} = C_{12}$.

5.2   Temperature Dependence of the Sound Velocity measured at Ambient Pressure

In order to perform the measurement of the sound velocity below room temperature, we used a 3methyl-1-butanol solution to keep the coupling between the transducer and

the sample. We put the sample-transducer assembly in a Teflon capsule filled with the same solution. This precaution was taken because the 3methyl-1-butanol solution is very volatile. The capsule was then inserted into the pressure cell. However, for the measurement at ambient pressure, no force was applied on the piston. During the experiment, the sound frequency $f(T)$ was measured as a function of temperature. To obtain the relative change in sound velocity, the data were normalized with respect to the frequency measured at room temperature $f(300)$,

$$\frac{\Delta f(T)}{f} = \frac{[f(T) - f(300)]}{f(300)} = \frac{\Delta v(T)}{v}. \tag{5.3}$$

As shown in chapter 4, this procedure is valid as long as the relative variation in the sample's length $\Delta L/L$ is small compared with $\Delta v/v$, see equation 4.8.

We present in Fig. 5.1 the temperature dependence of the relative change in sound velocity measured at ambient pressure for longitudinal modes propagating along the x-direction. The results have been obtained between 100 K and 300 K for one cooling-heating cycle. One can see from figure 5.1 that the relative change in sound velocity increases approximately linearly upon cooling down to about 206 K, and then it rapidly decreases. Between 188.2 K and 187.7 K, the velocity slightly increases before it decreases again even more rapidly. Finally, it increases monotonically with further cooling down to 100 K. For the heating process, the relative change in velocity decreases in the temperature range between 100 and 195 K. At 195.2 K, there is a sudden change in the sound velocity. Continuing the heating process, the next pronounced change in sound velocity occurs in the temperature range between 250 and 275 K. Finally, the velocity decreases as we warm the sample back to room temperature. Because the phase transition observed at 195.2 K is very narrow, less than 0.1 K, it was impossible to monitor the velocity change within that transition. Consequently, the curve for the heating process was adjusted relative to the data

Figure 5.1: Temperature dependence of the relative change in sound velocity in LiKSO$_4$ for longitudinal waves propagating along the x direction

obtained during the cooling process. The low temperature part was adjusted relative
to the value obtained at 130 K, while the high temperature section was positioned
relative to the value obtained at room temperature.

From the cooling-heating cycle presented in Fig. 5.1, we clearly distinguish two
phase transitions with very significant thermal hysteresis. This confirms that both
transitions are first order phase transitions. For that reason, all measurements around
the phase transitions have been obtained using a slow cooling, 0.1 K/min. In this
work, the transition temperatures were defined as

$$T_c = \frac{T[0.9(\frac{\Delta v}{v})_{max}] + T[0.1(\frac{\Delta v}{v})_{min}]}{2} \qquad (5.4)$$

where the transition is bounded by two extreme points [T $[(\Delta v/v)_{max}]$, $(\Delta v/v)_{max}$]
and [T[$(\Delta v/v)_{min}$], $(\Delta v/v)_{min}$], as shown in Fig. 5.1. Based on this procedure, the
first transition is observed at 195 K and 260 K for the cooling and heating process,
respectively. We noticed that the velocity drops by 9 % from its value at 195 K
during the cooling procces. Considering that the linear thermal expansion $\Delta L/L$
along the x-axis drops by 0.6% at that temperature [32, 37], we are justified to ignore
that contribution in our determination of $\Delta v/v$. The magnitude of the change in the
velocity is comparable with the drop measured by B. F. Borisov et al. [71, 72], which
is also about 8%. Their results was obtained using a conventional pulse acoustic
technique at a frequency of 5 MHz under slow cooling and warming (0.2 K/min).
In addition to that, our results regarding the temperatures of the first transition
for the cooling-heating cycle compare well with their results. They observed the first
transition at 195 K and 260 K [71, 72]. However, other groups observed that transition
at different temperatures. For example, the temperature dependence of the elastic
constant C_{11} measured by Kabelka et al. [68] shows a pronounced steep change at
(207 ± 2) K on cooling and at (244 ± 2) K on heating. Also, Fujimoto et al. [26]

reported the transition around 210 K and 250 K from the temperature dependence of the permittivity measurement. Maezawa et al. [50] reported that this transition occurs at 215 K on cooling and 250 K on heating using the resonance-antiresonance study. Also, Sharma [6] reported that the first transition is a first order due to the discontinuous change of the thermal expansion coefficient observed at 178 K.

The second transition, which shows a drop of 3 % in the sound velocity, occurs at 185 K and 195 K for the cooling and heating process, respectively. Again, our results are consistent with results obtained by Borisov et al. [71, 72]. They observed that transition for a cooling-heating cycle at 185 K and 195 K, respectively. However, it shows up at 189 K and 195 K for the measurement of the permittivity [26] as a function of temperature at ambient pressure. Maezawa et al. [50] reported that the second transition occurs at 191 K and 198 K on cooling and heating, respectively. Again, it is clear that the reported transition temperatures do not exactly agree with each other. Possible causes of these discrepancies might include the thermal history of the sample, the overall quality of samples used, or different heating and cooling rates.

We present in Fig. 5.2 the temperature dependence of the relative change in sound velocity measured at ambient pressure for longitudinal waves propagating along the z-direction. The results were obtained between 130 K and 300 K for one cooling-heating cycle. One can see from this figure that the sound velocity increases approximately linearly on cooling from 300 K down to about 188 K, and then it decreases very rapidly at 188.4 K. Finally, it increases monotonically when cooling from 186 K down to 130 K. For the heating process, the velocity decreases in the temperature range between 130 K and 192 K. At 192.82 K, there is a sudden change in the sound velocity. Continuing the heating process, the next change in the sound velocity occurs in the temperature range between 254 K and 262 K. Finally, the velocity decreases as we
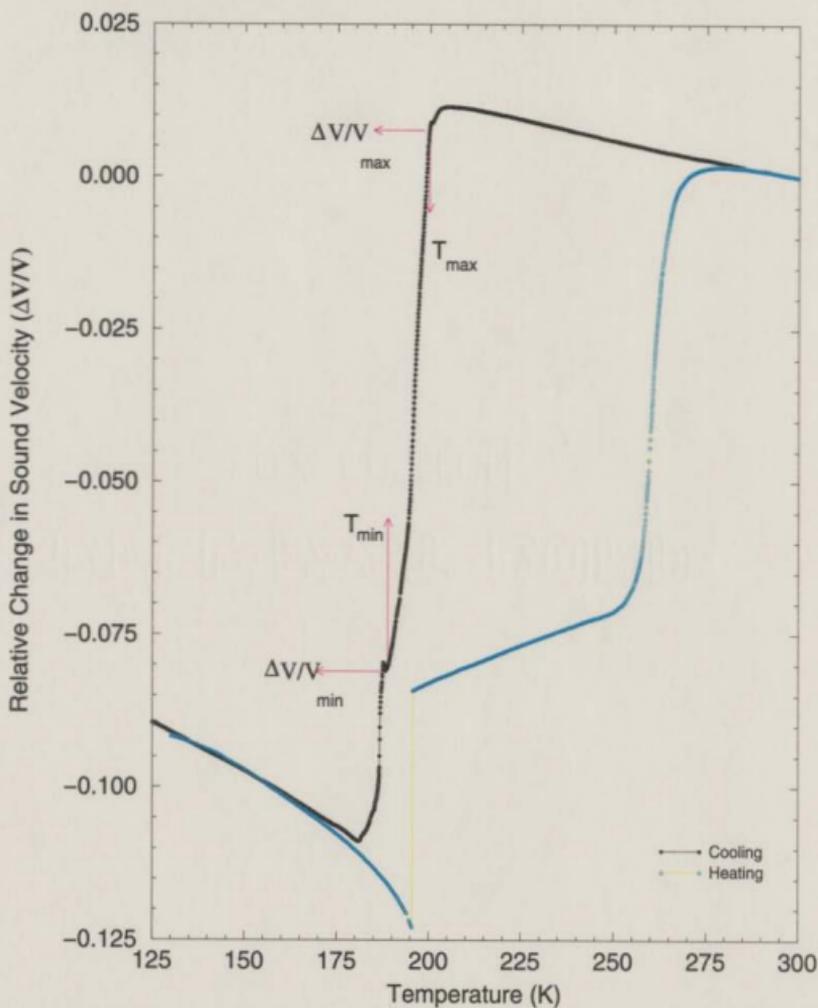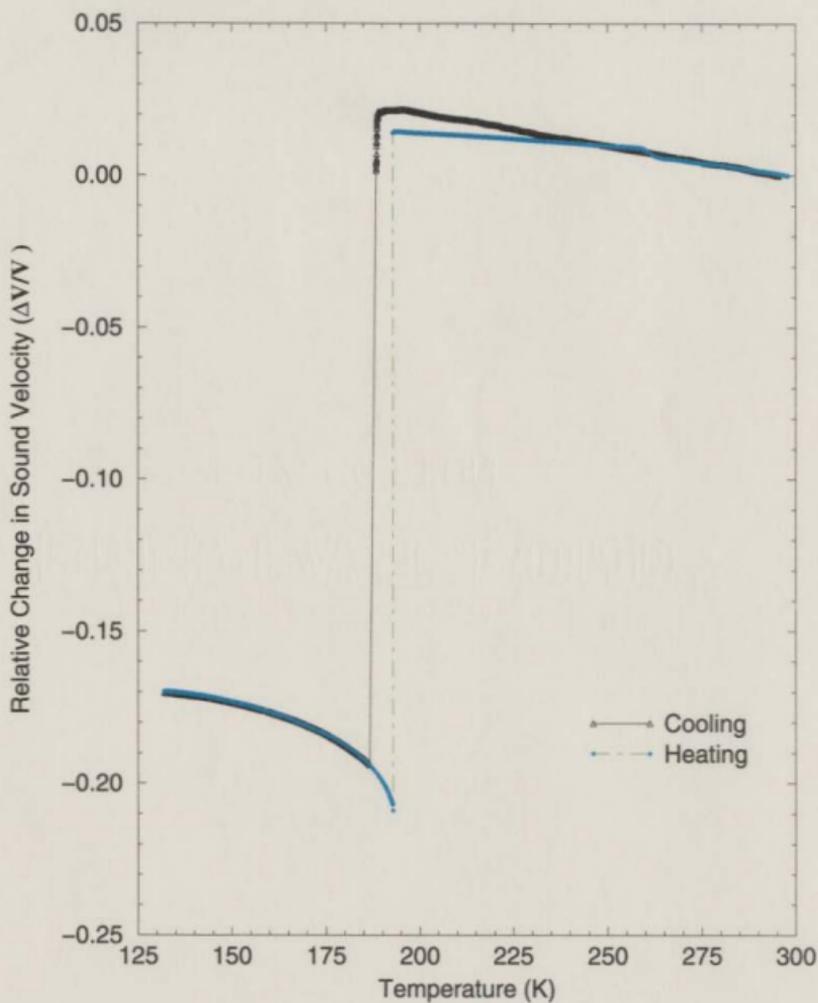
Figure 5.2: Temperature dependence of the relative change in sound velocity in LiKSO$_4$ for longitudinal waves propagating along the z-direction

warm up the sample to room temperature. Because the transitions observed at 188.4 K and 192.82 are very sharp, less than 0.1 K, it was impossible to monitor the velocity change within these transitions. Consequently, both parts of that curve have been adjusted using the values of the absolute sound velocity measured at room temperature and 190 K, respectively. In comparison with results obtained along the x-axis, we observe this time only one transition on cooling where the velocity drops by 22% at 187 K. However, for the heating process we still clearly identify two transitions, one at 193 K and an other at 258 K. Since, these critical temperatures scale well with what we have obtained along the x-axis, we can safely associate the transition at 187 K to the second transition observed along the x-axis during the cooling process, see Fig. 5.1. Similar results were obtained by Maezawa et al. [50] using a resonance-antiresonance method. They reported that the value of C_{33} changes remarkably at the second transition temperature, where T_c equal 191 K, while they did not notice any anomaly at the first transition temperature on cooling. They also observed two transitions on heating at 198 and around 250 K. Kabelka and Kuchler [68] measured C_{33} as a function of temperature using sound velocity measurements and observed a transition at 205 K and one at 190 K on cooling. In addition, the measurement of the lattice parameter c using X-ray diffraction [32, 37] shows two distinct transitions on cooling and two transitions at heating. This result is also corroborated by thermal dilatometry measurements by Fujimoto et al. [26]. The discrepancies in the results so far obtained may be attributed to the different crystals used in these experiments.

In general, our results for the temperature dependence of the sound velocity of longitudinal waves propagation along x or z-direction are comparable with results obtained by others for LiKSO$_4$ [2, 21, 52, 54, 68, 71, 72]. This confirms that our approach, where both the transducer and the sample are submerged in a 3methyl-1-butanol solution, gives reproducible and reliable results.

5.3 Pressure Effects on the Phase Transition in LiKSO$_4$

The behavior of LiKSO$_4$ under pressure has been the subject of only a small number of investigations [13, 24, 26, 76−79]. So far, the measurement of the dielectric and dilatometric properties have been realized up to a pressure of 8 kbar for temperatures between 150 K and 340 K [24, 26]. From these measurements, the authors have derived the pressure-temperature phase diagram of LiKSO$_4$ for the cooling-heating cycle. Raman scattering measurements at room temperature [76] have also been realized using a diamond anvil cell for pressure as high as 100 kbar. These results reveal three phase transitions labeled as $\alpha \underset{8kbar}{\overset{9kbar}{\rightleftarrows}} \beta \underset{10kbar}{\overset{30kbar}{\rightleftarrows}} \gamma \underset{49kbar}{\overset{67kbar}{\rightleftarrows}} \delta$. It is well established that the α phase at ambient pressure and room temperature corresponds to a hexagonal structure [77]. The structure of the β phase is still unresolved, however. Melo et al. [76] reported that it may be an incommensurate phase. The same authors also suggest that both γ and δ phases have closer packing where the latter probably belongs to a space group of lower symmetry than the ambient pressure α phase. Arora and Sakuntala [79] emphasised that the high pressure phases β, γ and δ appear to be different from low temperature phases PIV (the phase below the room temperature phase, some times called an intermediate phase), PV (the phase below 190 K), etc., because the Raman spectra of the low temperature phases are different from those obtained at high pressures. The transition from α to β at 9 kbar was confirmed by Sankaran et al. [78]. Further more, Sankaran et al. reported a novel solid-state crystal to amorphous transition at 120-150 kbar which was confirmed by Arora and Sakuntala [79].

There are also very few results at temperatures lower than 80 K on LiKSO$_4$. This is probably due to the difficulty of cooling samples without inducing defects. So
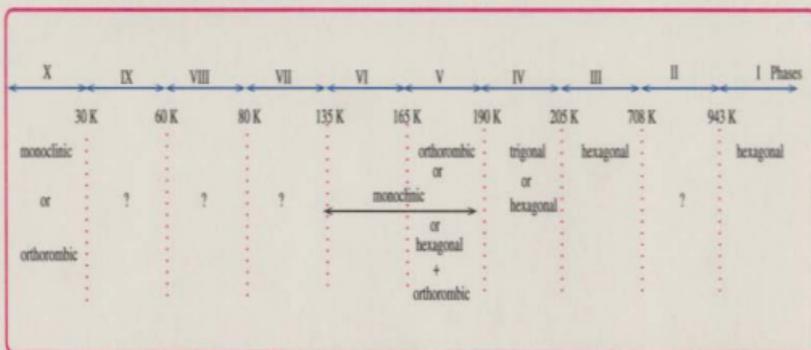
Figure 5.3: Sequence of phase Structures for LiKSO$_4$ on cooling

far, a few phase transitions have been observed by Raman scattering and dielectric studies [14, 80]. The reported transition temperatures are 20 K on cooling and 30 K on heating [14] and at 45 K on heating [80]. The pyroelectric coefficient and the dielectric constant show anomalous behavior occurring at 30 K [28]. Besides, Cach et al. [27, 99] observed anomalous behavior of the dielectric constant at 38 K, 53 K, 62 K, and 74 K, while Abello et al. [41] reported three transitions at 38 K, 65 K and 83 K. Diosa et al. [22] reported two transitions at 38 K and 57 K using heat-capacity measurements. Recently, Zhang et al. [74] reported that IR powder spectra show phase transitions near 35 and 60 K. From this point on, we will use the phase notation presented in Fig.[1] 5.3, we refer to the notation proposed by Perpetuo et al. and Desert et al. [37, 67] describing the sequence of phases, where P is the phase and the numbers give the temperature range for each phase, for example PIII is the room temperature phase, and so on.

---

[1]Here, we present Fig. 2.2 for convenience.

5.3.1   Pressure Dependence of the Relative Change in Sound Velocity at Ambient Temperature

The effect of pressure on the relative change in sound velocity of a longitudinal wave propagating along the x-axis of LiKSO$_4$ crystals was first investigated. Experiments were performed at room temperature, and the pressure was applied according to the procedure described in section 4.3. As shown in Fig. 5.4, the pressure dependence of

Figure 5.4: Pressure dependence of the relative change in sound velocity of the longitudinal modes propagating along the x-axis of LiKSO$_4$ crystals
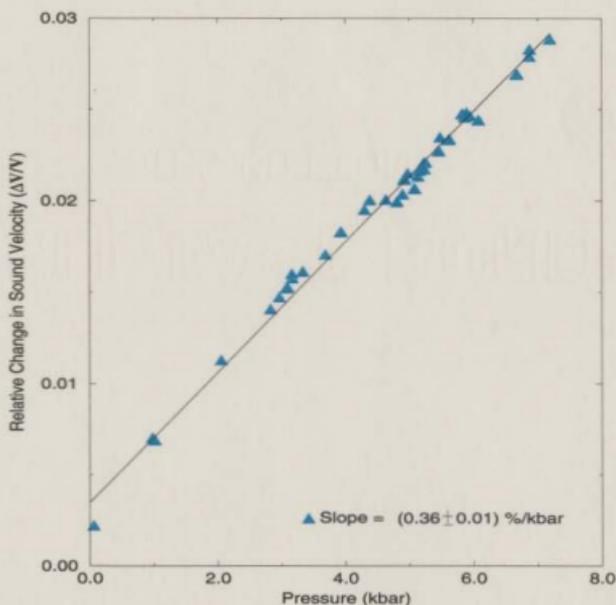
the relative change in sound velocity $\Delta v/v$, measured at room temperature, is well

represented by a linear relation with a slope of (0.36 ± 0.01) % per kbar. According to [76, 78], the first transition from α to β phase occurs at 9 kbar. Unfortunately we could not go up to 12 kbar to confirm the transition from α to β phase, which is believed to correspond to a transition from phase PIII to phase PV. For future work it is worthy to do measurements for pressures up to 12 kbar, where we expect to see the direct transition from phase PIII to phase PV. This is clear from the pressure-temperature phase diagram that we have obtained and which is presented in Fig. 5.6.

5.3.2   The Temperature-Pressure Phase Diagram

In this section, we present the temperature dependence of the relative change in sound velocity measured at different pressures for longitudinal modes propagating along the x-direction. The results presented in this section are limited to the temperature range between 130 K and 300 K. The measurements have been realized along the x-axis mainly because both transitions can be easily observed during the cooling and the heating process, see Fig. 5.1. Consequently, using these results, we can directly derive the pressure-temperature phase diagram of LiKSO$_4$ for temperatures between 130 K and 300 K. Furthermore, in order to compare the data obtained at different pressures, the same cooling (heating) rate, 0.1 K/min, has been used throughout the transition temperature ranges. This has been done to eliminate any effect of the cooling (heating) rate on the transition temperature. While discussing the data obtained here, we will refer to the notation presented in Fig. 5.3. In Fig. 5.5 (a) and (b), we present the temperature dependence of the relative change in sound velocity $\Delta v/v$ along the x-axis obtained at different pressures for the cooling and heating process, respectively. In Fig. 5.5 (a), we present the temperature dependence of the sound velocity at dif-
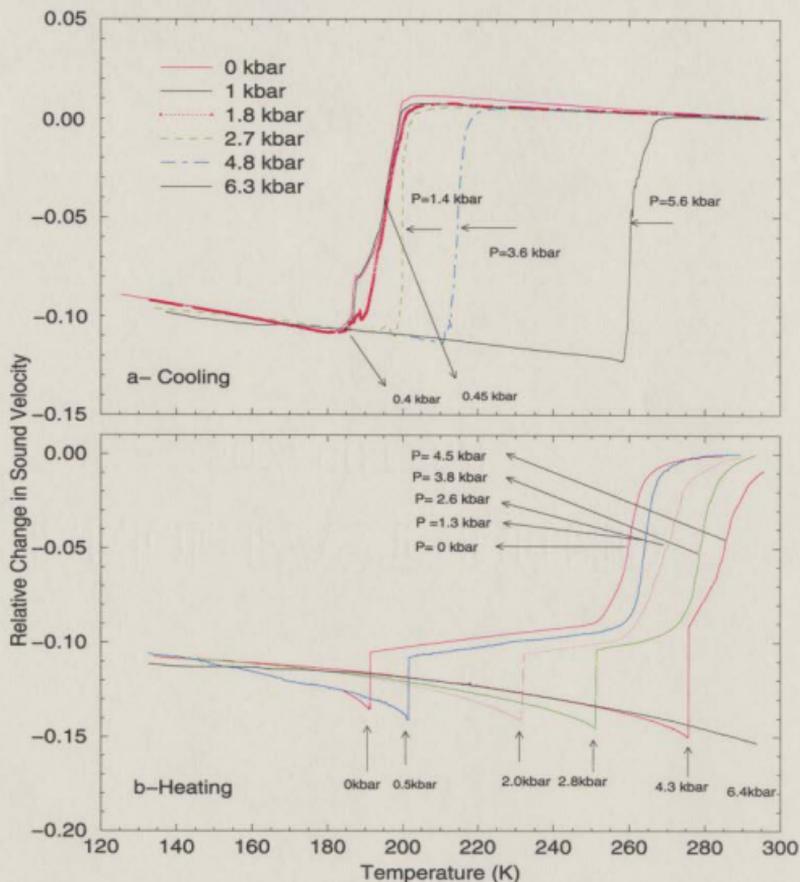
Figure 5.5: Temperature dependence of the relative change in sound velocity for longitudinal waves propagating along the x-axis at different pressures on cooling (a) and on heating (b). The pressure is measured at room temperature in Fig. 5.5 (a) and at the transition temperature in both figures

ferent pressures of the cooling process only. The pressure value in the legend was measured at room temperature, while the second value was measured at the transition temperature. The estimated error for the pressure is approximately ± 0.2 kbar. One can notice the decrease of pressure while cooling, due to the contraction of the pressure cell components. Hence, the curve which began with a pressure of 1 kbar at room temperature showed a pressure of 0 kbar at 200 K. Therefore, the transitions for the curve obtained at ambient pressure appear at the same temperatures as for measurements done at a pressure of 1 kbar at room temperature. In Fig. 5.5 (b), the pressure was also measured at the transition temperatures. The main feature of this figure is the shift of both transition temperatures towards higher temperatures with increasing pressure. For pressures less than (1.8 ± 0.2) kbar, one can see one transition from PIII to PIV and one from PIV to PV on cooling. However, for pressure greater than 1.8 kbar, we observe only one transition. It is clear that the intermediate phase PIV vanishes completely for pressures larger than (1.8 ± 0.2) kbar on cooling and greater than (5.0 ± 0.2) kbar on heating. Therefore, whenever the pressure is larger than those mentioned previously, the transition occurs directly between phase III and phase V. Finally, at 6.4 kbar, the transition temperature on heating is larger than 300 K so we could not observe the transition. From the above results and the data extracted from similar experiments at different pressures, the temperature-pressure phase diagram of LiKSO$_4$ was derived. Fig. 5.6 (a) and (b) show the temperature-pressure phase diagram for the cooling and heating, respectively. It is clear from Fig. 5.6 (a) that the intermediate phase PIV range of existance decreases with increasing pressure and disappears at pressures larger than the pressure of the triple point [(1.8 ± 0.2) kbar, (200 ± 1) K]. Beyond the triple point, there is only a transition from PIII to PV during cooling. Similar features are obtained during the heating process with the exception that the coordinates of the triple point are higher [(5.0 ± 0.2)
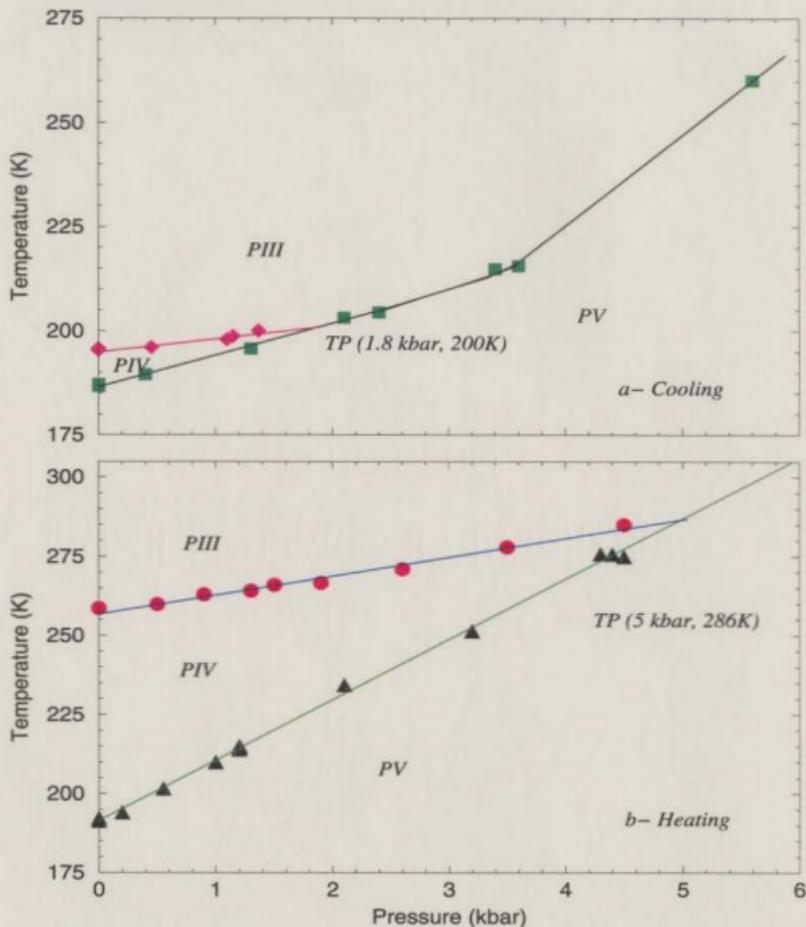
Figure 5.6: The temperature-pressure phase diagram of LiKSO$_4$ for cooling (a) and heating (b), with triple points at $(1.8 \pm 0.2$ kbar, 200 ± 1 K) and $(5.0 \pm 0.2$ kbar, 286 ± 5 K).

kbar, (286 ± 5) K]. As mentioned previously in section 5.2, all these transitions are first order transitions, and this has been confirmed by different groups even though they used different approaches. For example, the transition from room temperature phase III to the intermediate phase IV is reported to be first order. [10, 11, 48, 50, 72] and the transition from PIV to PV is also first order phase transition [6, 9]. The phase boundaries (in the temperature-pressure phase diagram) are represented by a linear function, except the curved boundary between PIII and PV in Fig. 5.6 (a). However, in order to compare our result with previous results reported by Fujimoto et al. [24, 26], these boundaries can be roughly represented by a linear relation. The slope of each boundary line is given in Table 5.3 with results obtained by Fujimoto et al. [24, 26]. Our results compare well with results obtained by measuring the pressure dependence of the strain $\Delta l/l$ along the c-axis of the LiKSO$_4$ crystals [25, 26]. We identify three distinct phases in the temperature range between 130 K and 300 K when the magnitude of the applied pressure is less than the pressure of the triple point. We also confirm (1) the shift of the transition temperature to higher values as pressure is increased, (2) the stability range of the intermediate phase IV decreases as the pressure rises and disappears for pressure above the triple point, and (3) the triple point for the cooling cycle is different from that for the warming process. So the results of the present work and the data obtained by Fujimoto et al. are comparable. Finally, from the phase diagram Fig. 5.6 (a) and (b), the crystal transforms from the α phase to the β phase at 8.3 ± 0.5 kbar and at 5.8 ± 0.5 kbar on increasing/ decreasing pressure at room temperature, respectively. This result also compares well with results found by [76, 78].

Comparison Type		Present Work	Fujimoto 1984	Fujimoto 1985
Triple Point	Cooling	(1.8 kbar, 200 K)		(2.1 kbar, 214K)
	Heating	(5.0 kbar, 286 K)	(4.3 kbar, 288 K)	(4.3 kbar, 290 K)
Slope of the	PIII to PIV	3.0±0.4		2.2±0.4
line separates	PIV to PV	7.6±0.3		12.0±0.3
between two	PIII to PV	16±2		11.2±0.3
phases dT/dP	PIV to PIII	5.9±0.3	8.3	9.0±0.3
in K/kbar	PV to PIV	19.1±0.2	21.7	22.2±0.2

Table 5.3: A comparison of the present work with previous results on the phase diagram of LiKSO$_4$.

5.3.3   Phase Transitions in the 4-300 K Range

Our initial attempts to measure the temperature dependence of the sound velocity below 80 K and ambient pressure all failed because of the breakdown of the mechanical coupling between the transducer and the sample. This problem here may arise from the stress that builds up between the transducer and the sample. This can be ascribed to the large thermal expansion of the sample, especially in the vicinity of a phase transition. We also notice that the sample shows many cracks or fissures whenever they were cooled down below 20 K at ambient pressure. In order to reduce these problems, we decided to perform the low temperature experiments with the sample always under some hydrostatic pressure. Fig. 5.7 shows one complete run where we successfully cooled the sample down to 4 K and warmed it back to room temperature. Here, we will discuss the behavior of the sound velocity as a function of temperature between 80 K and 300 K. Then we will focus on the transitions below 80 K. For this run, the hydrostatic pressure at 292 K was 3.7 ±0.2 kbar, however it decreases

gradually with cooling due to the thermal contraction of the pressure cell and the piston. Thus, the pressure at the transition observed at 203 ±1 K was down to 2.1 ±0.2 kbar. According to our phase diagram in figure 5.6, this corresponds to a transition directly from PIII to PV. Below 120 K we assume that the pressure remains constant at 1 ±0.2 kbar since the pressure medium inside the Teflon cell is completely frozen. For the warming process, we observe two transitions: the transition from phase PV to phase PIV occured at 252 ±1 K at 3.2 ±0.2 kbar and the transition from PIV to PIII is observed at 277 ±1 K for a pressure of 3.5 ±0.2 kbar. Again, these results are consistent with our phase diagram presented in figure 5.6 even after the sample was cooled down to 4 K. Moreover, our visual inspection of the sample, even after many thermal cycling down to 4 K, did not reveal any sign of defects or cracks within the crystal. Below 80 K, we observed two transitions, one at 64.4 ± 0.5 K and another at 37.7 ± 0.5 K for a pressure of 1 ±0.2 kbar. Furthermore, even if the cooling /heating rate is 0.5 K/min, we did not observe a significant thermal hysteresis effect for these two transitions below 80 K. Our results agree with results obtained by J. E. Diosa al. [22]. Raman study by H. K. Liu et al. [80] confirmed a transition at 45 K while Ming Zhang et al. [74] observed transitions at 35 K and 60 K using infrared spectroscopic study.

We present in Fig. 5.8 the temperature dependence of the relative change in sound velocity measured at different pressures for the longitudinal wave propagating along the x-axis in the temperature range between 4 K and 80 K (these curves have been shifted for an easier comparison). It is clear from the curve measured at 1 kbar that the velocity increases montonically upon cooling from 80 K to 70 K, and then at 68 K it rapidly decreases. Between 63 K and 40 K the velocity increases as the temperature is decreased, then it increases again more rapidly in the 33-40 K range. Finally between 4 K and 33 K it increases again. As shown in Fig. 5.8,

we notice a decrease in the velocity variation around 35 K with increasing pressure. This transition disappears for pressures greater than 3 kbar. The drop in velocity observed around 65 K is also pressure dependent, but there is no significant effect on the transition temperature with increasing pressure. Our results obtained so far confirm the existence of the phases III, IV, V, VIII, IX and X, because we observed four transitions in the temperature range between 4 K and 300 K, at 205 K, 187 K. 65 K and 35 K on cooling. Furthermore, we did not observe any transition at 165 K. 135 K and 80 K, so we cannot confirm any transition between 80 K and 160 K, see Fig. 6.1.

Figure 5.7: Temperature dependence of the relative change in sound velocity for a longitudinal wave propagating along the x-axis of LiKSO$_4$ crystal.
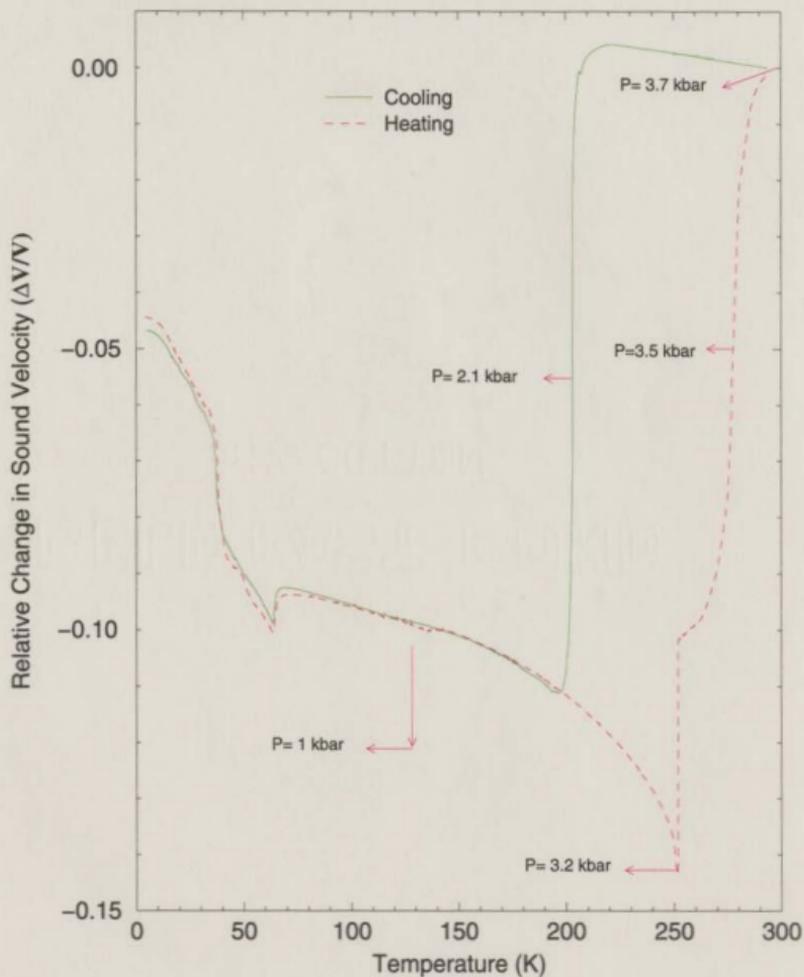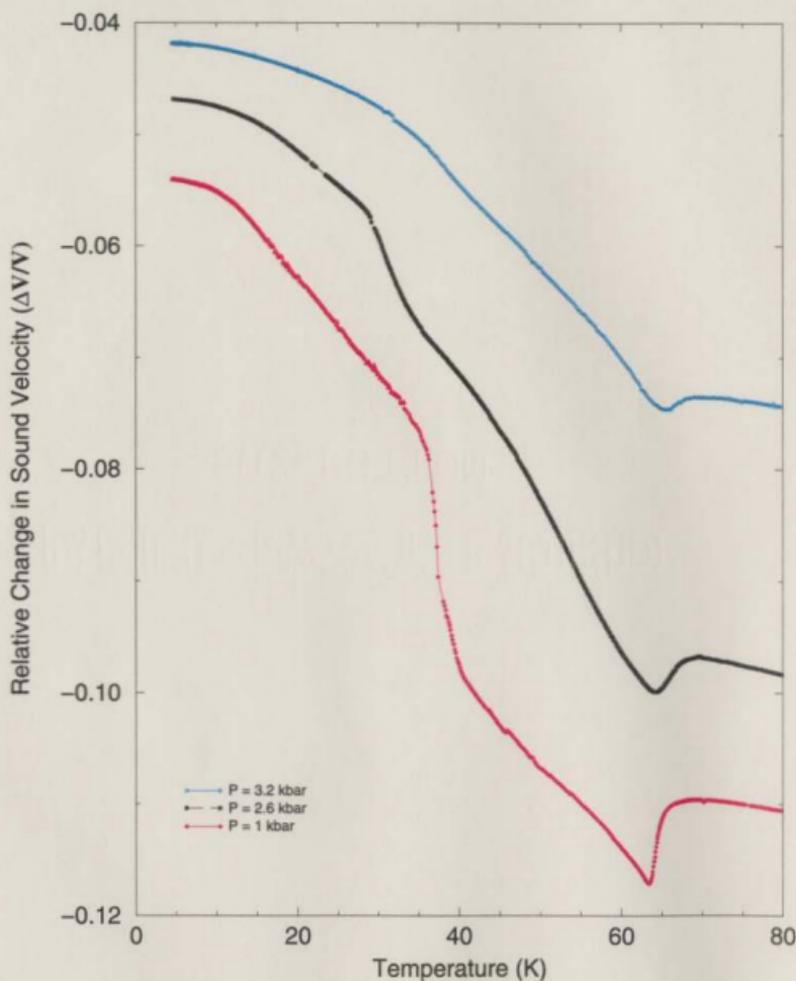
Figure 5.8: Temperature dependence of the relative change in sound velocity for the longitudinal wave propagating along the x-axis of LiKSO$_4$ at different pressures.

Chapter 6

Conclusions

The main goal of all the experiments done in this thesis was to gain a better understanding of the physical properties of LiKSO$_4$ crystals. In particular, a major focus was on understanding the phase transitions of LiKSO$_4$ crystal, and the effects of pressure and temperature on the sound velocity propagating along the x and z axes. This chapter summarizes and concludes the work presented in this thesis.

6.1 Conclusion

The main conclusions of this work are the following using the pulse echo method four of the seven transition points listed in the introduction were observed. Thus, the existence of the phases III, IV, V, IX and X were confirmed in the range between 4 K and 300 K, as shown in Fig. 6.1. At ambient pressure, our results show distinct phase transitions at 195 K, 185 K, 65 K, and 35 K on cooling and at 35 K, 65 K, 195 K, and 260 K on heating. There was no transition observed between 70 K and 180 K, therefore we cannot confirm the transition observed in this range by other groups using different methods. Based on this, we modify the phase sequence of the transitions to be as shown in Fig. 6.1. The phase transitions show thermal hysteresis on successive heating and cooling cycles between 130 K and 300 K, while
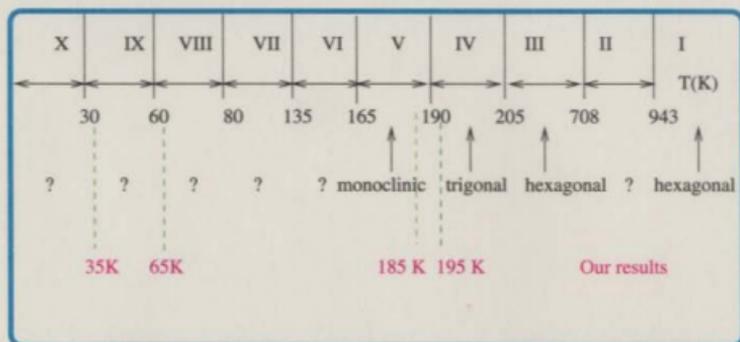
Figure 6.1: Sequence of phases compared to our results

the transitions between 4 K and 80 K do not show this effect.

Our results indicate that the longitudinal sound velocity for propagation along the x-axis and z-axis shows anomalous changes in its values at about the same temperatures on cooling and heating. This may be due to the elastic properties in this range. We cannot confirm the structures of these phases because our results are not sufficient for this purpose.

As proved by Bhakay-Tamhane et al. [44], the total crystal does not undergo transformation at any of the transition temperatures, but exhibits mixed phases. Accordingly, we noticed also that the transition temperature T_c is shifted if the cooling or heating rate of the sample is changed. This is because the crystal needs a time to reach its equilibrium state (i.e. stabilization). A very low cooling or heating rate may be the best way to prevent the coexistence of different phases. The values of the elastic constants at the room temperature phase are in good agreement with earlier results obtained by other groups.

The temperature-pressure phase diagram in the 130-300 K range was obtained. Its main features are: (1) the existance range of phase IV decreases as the pressure increases and vanishes at a triple point on cooling and heating, (2) the triple points

are $(1.8 \pm 0.2$ kbar, 200 ± 1 K$)$ and $(5.0 \pm 0.2$ kbar, 286 ± 5 K$)$ for cooling and heating, respectively, (3) with increasing pressure, the transition temperature is shifted to higher values for the range 130-300 K. In contrast, increasing pressure does not shift the transition temperature for the transitions below 80 K, but it does decrease the change in sound velocity at the transition. As a result, we do not observe the transition from phase PIX to phase PX if the pressure is greater than 3.2 kbar. A complete pressure-temperature phase diagram in the range between 4 K and 300 K is presented in Fig. 6.2, where the dashed lines represent the expected dependence and the x mark means the end of the phase boundary where we do not detect a phase transition at pressures greater than 3.2 kbar.

6.2 Suggestions for Further Work

More experiments are needed in order to confirm the crystal structures, especially experiments in the range 4-300 K for the longitudinal mode in the x and y directions. In order to find the complete set of the elastic constants, we need to do experiments in the [101] or [011] direction.
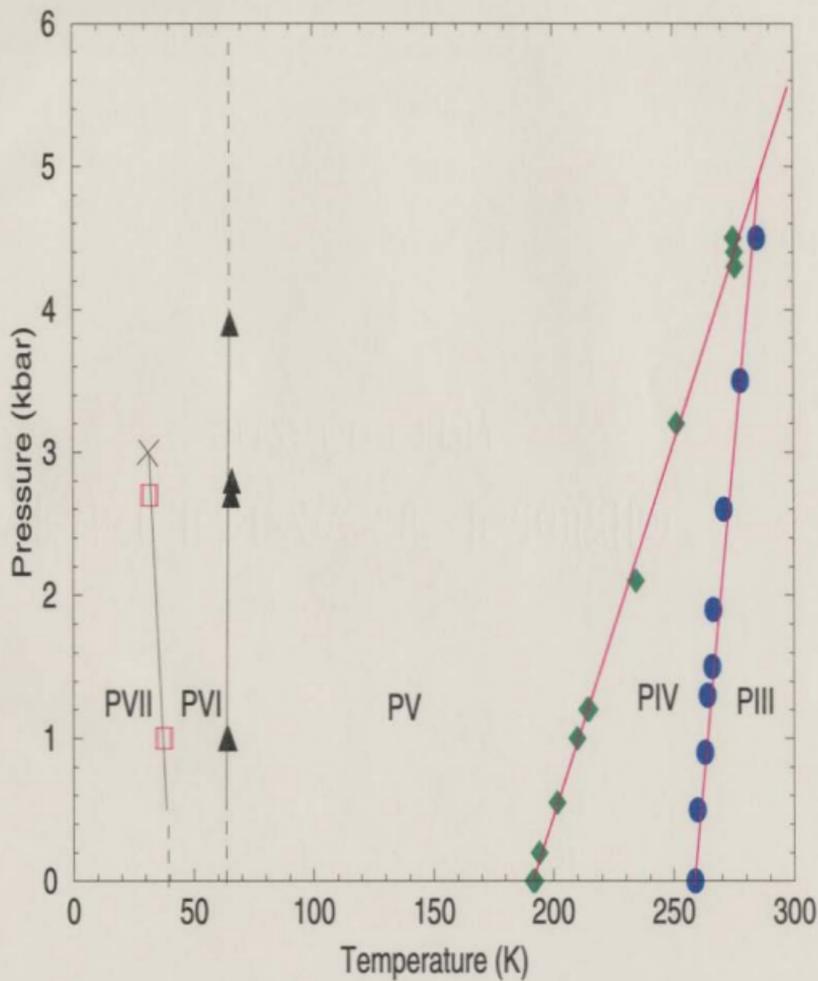
Figure 6.2: Pressure-temperature phase diagram of LiKSO$_4$

Bibliography

[1] P. E. Tomaszewki, *test*, J. Sol. State Chem. **156**, 253 (2001).

[2] M. Drozdowski and F. Holuj, , Ferroelectrics **77**, 47 (1988).

[3] B. Mroz, T. Krajewski, and T. Breczewski, , J. Physics Condens Matter **1**, 5965 (1989).

[4] M. A. Pimenta, P. Echegut, Y. Luspin, G. Hauret, and F. Gervais, , Phys. Rev. B **39**, 3361 (1989).

[5] F. Willis, R. G. Leisure, and T. Kanashiro, , Phys. Rev. B **54**, 9077 (1996).

[6] D. P. Sharma, , Pramana **13**, 223 (1979).

[7] R. Ando, , J. Phys. Soc. Japan **17**, 937 (1962).

[8] T. Rao, M. Bansal, V. Sahni, and A. Roy, , Phys. Sata. Sol(b) **75**, K31 (1976).

[9] M. L. Bansal, S. K. Deb, A. P. Roy, and V. C. Sahni, , Solid State Commun. **36**, 1047 (1980).

[10] A. J. Oliveira, F. A. Germano, J. Mendes Filho, F. E. A. Melo, and J. E. Moreira, , Phys. Rev. B **38**, 12633 (1988).

[11] M. L. Bansal and A. P. Roy, , Phys. Rev. B **30**, 7307 (1984).

[12] R. L. Moreira, , Phys. Rev. Sec. B **52**, 12591 (1995).

[13] K. Akhilesh and T. Sakuntala, , Phys.Condens. Matter **4**, 8697 (1992).

[14] J. Mendes Filho, J. E. Moreira, F. E. A. Melo, F. A. Germano, and A. S. B. Sombra, , Solid State Commun. **60**, 189 (1986).

[15] F. Ganot, B. Kihal, R. Farhi, and P. Moch, , Japanese Journal of Applied Physics **24-2**, 491 (1985).

[16] F. Ganot, B. Kihal, C. Dugautier, R. Farhi, and P. Moch, , J. Phys. C **20**, 4491 (1987).

[17] M. Drozdowski, F. Holuj, and M. Czajkowski, , Solid State Communicattions **45**, 1005 (1983).

[18] P. W. Young, R. S. Katiyar, and J. F. Scott, , Journal of Raman Spectroscopy **15**, 347 (1984).

[19] M. A. Pimenta, P. Echegut, and F. Gervais, , J. Phys. C **19**, 5519 (1986).

[20] M. A. Pimenta, Y. Luspin, and G. Hauret, , Solid State Commun. **62**, 275 (1987).

[21] T. An, L. Jing-qing, G. Ben-yuan, M. Yu-jun, Y. Hua-guang, and W. Yan-yup, , Solid State Commun. **61**, 1 (1987).

[22] J. E. Diosa, G. Gonzales-Montero, and R. A. Vargas, , Phys. Status Solidi **220**, 647 (2000).

[23] T. Breczewski, T. Krajewski, and B. Mroz, , Ferroelectrics **33**, 9 (1981).

[24] S. Fujimoto, N. Yasuda, and H. Hibino, , Physics Letters A **104**, 42 (1984).

[25] S. Fujimoto, N. Yasuda, H. Hibino, and P. S. Narayanan, , J. Phys. D **17**, L35 (1984).

[26] S. Fujimoto, N. Yasuda, and H. Hibino, , J. Phys. D **18**, 1871 (1985).

[27] R. Cach, P. Tomaszewski, and J. Bornarel, , J. Phys. C **18**, 915 (1985).

[28] R. C. de Sousa *et al.*, , Solid State Commun. **87**, 959 (1993).

[29] A. J. Bradley, , Phil. Mag. **49**, 1225 (1925).

[30] T. R. Prasad, Y. C. Venudhar, L. Iyengar, and K. V. Krishna Rao, . Pramana **11**, 81 (1978).

[31] P. E. Tomaszewski and K. Lukaszewicz, , Phys. Status Solidi A **71**, K53 (1982).

[32] P. E. Tomaszewski and K. Lukaszewicz, , Phase Transitions **4**, 37 (1983).

[33] M. Karppinen, , Acta Crystallogr. C **39**, 34 (1983).

[34] Y. Y. Li, , Solid State Commun. **51**, 355 (1984).

[35] H. Schulz, U. Zucker, and R. Frech, , Acta Crystallogr. Sec. B **41**, 21 (1985).

[36] R. H. Chen and R. T. Wu, , J. Phys. C **1**, 6913 (1989).

[37] A. Desert, A. Gibaud, A. Righi, U. A. Leitao, and R. L. Moreira, , J. Phys. C **7**, 8445 (1995).

[38] D. R. Ventura, N. L. Speziali, and M. A. Pimenta, , Phys. Rev. B **54**, 11869 (1996).

[39] S. Xavier, M. Calvet, M. Martinez-Saaion, L. Mestres, A. Bakkali, E. Bocanegra, J. Mata, and M. Herraiz, , J. Sol. Stat. Chem. **148**, 316 (1999).

[40] S. Xavier, M. Calvet, M. Martinez-Saaion, L. Mestres, A. Bakkali, E. Bocanegra, and M. Mata, J. andHerraiz, , J. Sol. Stat. Chem. **156**, 251 (2001).

[41] L. Abello, K. Chhor, and C. Pommier, , J. Chem. Thermodynamics **17**, 1023 (1985).

[42] I. M. Iskornev, I. N. Flerov, M. V. Gorev, L. A. Kot, and V. A. Grankina. , Soviet Phys:Solid State **26**, 1926 (1984).

[43] S. Bhakay-Tamhane, A. Sequeira, and R. Chidambaram, , Solid State Communication **53**, 197 (1985).

[44] S. Bhakay-Tamhane and A. Sequeira, , Ferroelectrics **69**, 241 (1986).

[45] G. Eckold, T. Hahn, and G. Krexner, , Phase Transitions **8**, 335 (1987).

[46] A. M. Balagurov, B. Mroz, N. C. Popa, and B. N. Savenko, , Phys. Status Solidi A **96**, 25 (1986).

[47] P. L. Zhang, Q. W. Yan, and J. X. Boucherle, , Acta Crystallogr. C **44**, 592 (1988).

[48] S. Bhakay-Tamhane, A. Sequeira, and R. Chidambaram, , Phase Transitions **33**, 75 (1991).

[49] C. Scherf, W. Paulus, G. Heger, and T. Hahn, , Physica B **276-278**, 247 (2000).

[50] K. Maezawa, H. Takeuchi, and K. Ohi, , J. Phys. Soc. Jap. **54**, 3106 (1985).

[51] T. R. Shibata and M. Fukui, , J. Phys. Soc. Japan **55**, 2088 (1986).

[52] B. Mroz, T. Krajewski, and T. Breczewski, , Ferroelectrics **42**, 71 (1982).

[53] A. R. Lim and S.-Y. Jeong, , Phys. Status Solidi B **207**, 81 (1988).

[54] T. Krajewski, T. Breczewski, M. Kassem, and B. Mroz, , Ferroelectrics **55**, 143 (1984).

[55] T. Krajewski, T. Breczewski, P. Piskunowicz, and B. Mroz, , Ferroelectrics Letters **4**, 95 (1985).

[56] W. Kleemann, F. J. Schafer, and A. S. Chaves, , Solid State Commun. **64**, 1001 (1987).

[57] U. A. Leitao, A. Righi, P. Bourson, and M. A. Pimenta, . Phys. Rev.B **50**, 2754 (1994).

[58] N. K. Madi, M. Kassem, M. M. El-Muraikhi, and A. El-Khatib, , Matterials Letters. **97**, 431 (1999).

[59] G. Sorge and H. Hempel, , Phys. Status Solidi A **97**, 431 (1986).

[60] B. Topic, U. Haeberlen, and R. Blinc, , Z. Phys. B **70**, 95 (1988).

[61] F. Holuj and M. Drozdowski, , Ferroelectrics **36**, 379 (1981).

[62] C. H. A. Fonseca, G. M. Ribeiro, R. Gazzinelli, and A. S. Chaves, . Solid State Commun. **46**, 221 (1983).

[63] J. T. Yu and S. Y. Chou, , J. Phys. Chem. Solids. **47**, 1171 (1986).

[64] J. T. Yu, J. M. Kou, S. J. Huang, and L. S. Co, , J. Phys. Chem. Solids. **47**, 121 (1986).

[65] K. Murthy and S. V. Bhat, , J. Phys. C. Solid State Physics **21**, 597 (1988).

[66] H. Bill, Y. Ravi Sekhar, and D. Lovy, , J. Phys. C **21**, 2795 (1988).

[67] G. J. Perpetuo, M. S. S. Dantas, R. Gazzinelli, and M. A. Pimenta, , Phys. Rev. B **45**, 5163 (1992).

[68] H. Kabelka and G. Kuchler, , Ferroelectrics **88**, 93 (1988).

[69] E. V. Charnaya, B. F. Borisov, T. Krajewski, and A. K. Radjabov, , Solid State Commun. **85**, 443 (1993).

[70] B. F. Borisov, E. V. Charnaya, and A. K. Radzhabov, , Phys. Status Solidi B **181**, 337 (1994).

[71] B. F. Borisov, E. V. Charnaya, and A. K. Radzhabov, , Ferroelectrics **185**, 161 (1996).

[72] B. F. Borisov, E. V. Charnaya, and M. Y. Vinogradova, , Phys. Stat. sol. b **199**, 51 (1997).

[73] L. Godfrey and J. Philip, , Sol. Stat. Commun. **97**, 635 (1996).

[74] M. Zhang, E. K. H. Salje, and A. Putnis, , J. Phys. C **10**, 11811 (1998).

[75] N. Choudhury, , Phys. Rev. Sec. B **33**, 8607 (1986).

[76] F. Melo, V. Lemos, F. Cerdeira, and J. M. Filho, , Phys. Rev. B. **35**, 3633 (1987).

[77] H. Sankaran, S. Sikka, M. Surinder, and R. Chidambaram, , Phys. Rev. B **38**, 170 (1988).

[78] H. Sankaran, S. K. Sikka, A. Sequeira, and B. Fursenko, , Bull. Mater. Sci. **14**, 1213 (1991).

[79] K. Akhilesh and T. Sakuntala, , Solid State Communications **75**, 855 (1990).

[80] H. K. Liu, M. L. Hu, W. S. Tse, D. P. Wong, and S. J. Lin, , Chinese Journal of Physics **36**, 542 (1998).

[81] M. D. Sastry, A. G. I. Dalvi, and M. L. Bansal. , J. Phys. C **20**, 1185 (1987).

[82] B. Mroz, T. Krajewski, and T. Breczewski, , Acta Phys. Pol. A **63**, 445 (1983).

[83] V. I. Stadnik, N. A. Romanyuk, R. S. Brezvin, and V. I. Karash, , Crystallography Reports **42**, 660 (1997).

[84] G. Gordoetsky and I. Lachterman, , Re. Sci. Instrum. **52**, 1386 (1981).

[85] H. B. Huntington, , Phys. Rev. **72**, 321 (1947).

[86] D. Lazarus. , Phys. Rev. **10**, 545 (1949).

[87] S. Eros and J. R. Reitz, , The Journal of Applied Physics **29**, 683 (1957).

[88] L. D. Landau and E. M. Lifshitz, *Theory of Elasticity* (Pergamon Press. Oxford, 1986).

[89] C. Kittel, *Introduction to Solid State Physics* (John-Wiley and Sons. New York, 1996).

[90] E. Dieulesaint and D. Royer, *Elastic Waves in Solids. Application to Signal Processing* (John Wiley & Sons Ltd., Chechister, 1980).

[91] E. Schreiber, O. Anderson, and N. Soga, *Elastic Constants and Their Measurements* (McGraw-Hill, New York, 1973).

[92] C. N. Rao and K. J. Rao, *Phase Transitions in Solids* (Mc Graw-Hill, New York, 1978).

[93] G. Burn, *Solid State Physics* (Academic Press, London, 1985).

[94] W. P. Mason and R. N. Thurston, *Physical Acoustic VIII* (Acadimic Press, London, 1971).

[95] W. P. Mason and R. N. Thurston, *Physical Acoustic XII* (Acadimic Press, London, 1976).

[96] W. P. Mason and R. N. Thurston, *Physical Acoustic I Part A* (Acadimic Press, London, 1964).

[97] M. Eremets, *High Pressure Experimental Methods* (Oxford Science Publications, Oxford, 1996).

[98] J. Witting, A. Eichler, and Z. Angew, , Physica **25**, 319 (1968).

[99] R. Cach, P. Tomaszewski, P. Bastie, and J. Bornarel, , Ferroelectrics **53**, 337 (1984).